Spin Flop in Tetragonal Phase CuMnAs Antiferromagnets

James Felton & Stu Poole

June 1, 2018

Abstract

We explore some of the properties of the antiferromagnetic material CuMnAs. This is done through a combination of spin-flop measurements, zero field anisotropic resistance measurements and a series of numerical models. The spin flop field is measured in CuMnAs to be $B_{\text{sf}} = 1.48 \pm 0.04\text{T}$ for one of our material samples, and $B_{\text{sf}} = 1.44 \pm 0.04\text{T}$ for the other. The results from these works, when combined with XMLD-PEEM images, were used to determine the exchange energy density and anisotropic energy density in CuMnAs in two limits. The first model, derived by considering two moments in free space, yielded an exchange field strength of $220 \pm 50\text{T}$ and anisotropy field strength of $5 \pm 2 \times 10^{-}3\text{T}$. The second model, considering a moments in the bulk, provided an exchange field of $80 \pm 20\text{T}$ and anisotropy field of $1.7 \pm 0.5 \times 10^{-}3\text{T}$. In the course of our project also obtained a number of simulation results applicable to antiferromagnets more widely.

Acknowledgements

We would like to thank the following members of the University of Nottingham Spintronics group for their assistance and efforts in this project. In particular we would like to thank Richard Campion for growing RC123, the wafer of CuMnAs used in this project. Similarly we would like to thank Mu Wang for his efforts and patience in etching, bonding and rebonding the two samples used, especially when a sample was dropped on day one. Thanks to Ollie Amin for helping to rebond the samples and for aiding with the high temperature rig. Thanks go to Kevin Edmonds and Peter Wadley for their enthusiasm and ideas throughout the project and for providing the XMLD-PEEM images of RC123 used in this report. Finally, a thanks to Bryan Gallagher for accommodating our decision to make the assigned project into a more experimental one, his insight and enthusiasm throughout and for being our supervisor on this complicated and insightful journey.

Contents

Introduction **4**

Theory **7**
Spin-Flop in Antiferromagnets . . . 7
Spin-Flop for Two Moments . . . 7
Spin-Flop in the Bulk . . . 8
Anisotropic Resistances . . . 10
Copper Manganese Arsenide . . . 11
Domain Wall Formation . . . 12
Dynamic Force Microscopy . . . 13

Experimental Methods **15**
Samples RC123 L1 and RC123 L2 . . . 15
Spin-Flop Measurements . . . 17
Alignment Investigations . . . 18
High Temperature Measurements . . . 19
Dynamic Force Microscopy Imaging . . . 20

Simulations **21**
Spin Flop Simulation Approach . . . 21
Domain Wall Simulation Approach . . . 22

Results **23**
Spin Flop and Alignment Results . . . 23
Temperature Variation Results . . . 25
Dynamic Force Microscopy Results . . . 28

Simulation Results **30**
Spin Flop Simulation Results . . . 30
Domain Wall Simulation Results . . . 32

Anisotropy and Exchange Strengths **35**

Discussion **36**

Summary **41**

Introduction

After ferromagnetic (FM) materials were discovered, they found uses in navigation, in industry as motors and generators and in many other applications. Eventually they found their way into early storage devices and now form the backbone of high density storage for computers worldwide. Antiferromagnetic (AFM) materials, by contrast, were not mathematically described until the 1940s by Néel, and and were thought to be of only theoretical interest [1]. In the following decades, research into AFMs remained dormant until the 1980s when discoveries of phenomena such as giant magnetoresistance and tunnelling magnetoresistance, among other effects [2, 3], lead to practical applications when used in conjunction with FMs. More recently AFMs have seen renewed interest as a stand alone material for spintronic applications, utilising spin-transfer torques, switching, and other effects [4, 5, 6, 7, 8]. In order to explain this resurgence in interest, we first need to introduce antiferromagnetism and what makes it so challenging to study, before describing our attempts to do so.

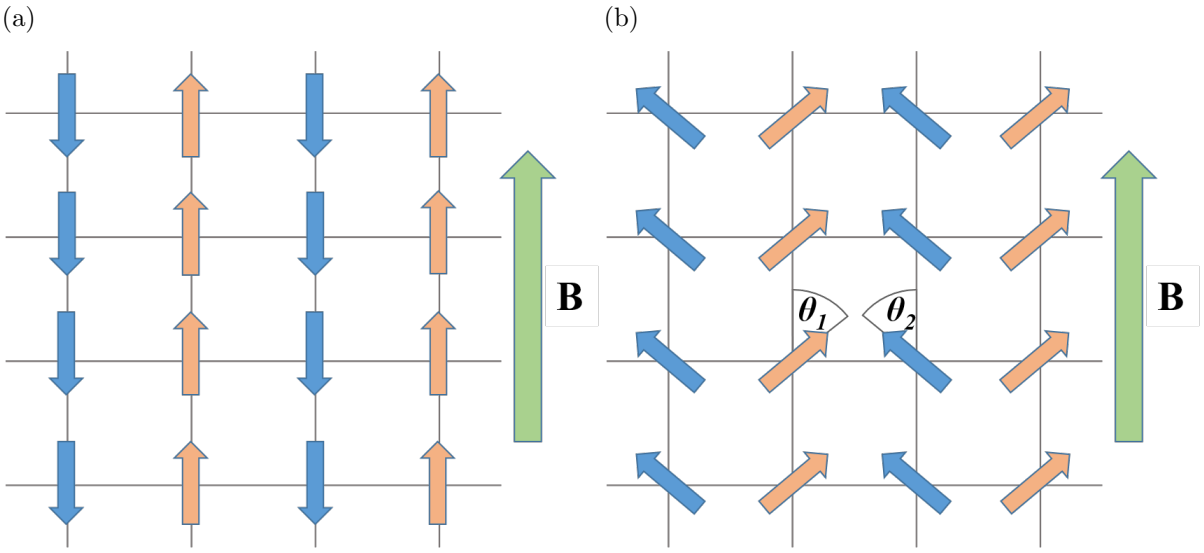

Figure 1: A schematic representation of the moments in the two AFM sublattices in a) the unflopped state and b) the flopped state, with the moments of each sublattice making angles θ_1 and θ_2 to the easy axis.

In both FMs and AFMs the interaction between magnetic moments is governed by an exchange interaction, this interaction between a moment i and its neighbours j is described by the Heisenberg model

$$\epsilon_i = \frac{1}{2}\sum_j A_{i,j}\mathbf{S_i}\cdot\mathbf{S_j} \tag{1}$$

where ϵ_i is the energy correction to moment i, $A_{i,j}$ is the exchange coupling strength between i and j, and $\mathbf{S_i}$ and $\mathbf{S_j}$ are the vector moments for i and j respectively. In FMs, $A < 0$ and as such the exchange interaction acts to align neighbouring moments parallel to one another. The opposite is true of AFMs which have $A > 0$ resulting in the anti-parallel configuration shown in Figure 1a being favourable. The two additional contributions to the energy are the anisotropy term and the Zeeman term. The anisotropy term acts to align the moments along a favourable crystallographic axis whilst the Zeeman term simply acts to align the moments with an externally applied field. With these three terms, the energy of a single moment, i, coupled to two neighbours, $i-1$ and $i+1$, in a one dimensional (1D) AFM crystal is

$$E_i = -MB\cos(\theta_i - \phi) + 0.5AM^2\cos(\theta_i - \theta_{i-1}) + 0.5AM^2\cos(\theta_i - \theta_{i+1}) - 0.5\Delta\cos^2(\theta_i), \tag{2}$$

where M is the magnitude of a single magnetic moment, B is the externally applied magnetic field, θ_i is the angle of the moment to the easy axis, ϕ is the angle of the external field to the easy axis, θ_{i-1} and θ_{i+1} are the angles of the two neighbouring moments to the easy axis, and Δ is the anisotropy strength. These variables are illustrated in Figure 2. In most AFMs, under reasonable conditions, the dominating contributions to Equation 2 come from the exchange terms, with the value of AM typically of the order of hundreds or thousands of Tesla [9, 10, 11], whereas the anisotropy, Δ/M, is typically very weak [12].

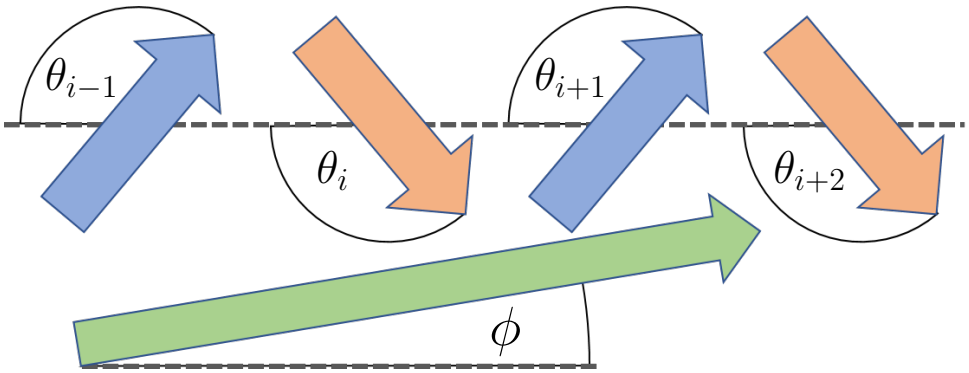

Figure 2: Schematic showing the relevant angles in Equation 2. The dashed lines represent the easy axis, the blue and orange arrows are those of the two moments in each sublattice, and the green arrow represents the applied B field.

The behaviour of AFM materials can be compared to that of their FM counterparts by considering the magnetisation of two interlaced sublattices, as represented by orange and blue in Figure 1a. With the system dominated by the exchange coupling, any phenomenon which acts to rotate the moments of the two sublattices in opposite directions is suppressed, whereas any interaction which acts to rotate them in the same direction is represented in AFMs the same as it is in FMs. This can be considered as part of a general principle with regard to AFMs, whereby phenomena which are an even function of sublattice magnetisation in FMs are equally present in AFMs, whereas those which are an odd function of sublattice magnetisation are suppressed [13]. Accordingly, AFMs exhibit much lower susceptibilities than FMs, with a greater dependence on field orientation (at low fields). Net magnetisation is, of course, an odd function of sublattice magnetisation and as such AFMs don't produce stray fields.

The lack of stray fields and the low magnetic susceptibility of AFMs meant they were traditionally only viewed as being of theoretical interest, with little to no practical applications. But the past thirty years has seen a renewed interest in AFMs as people have come to realise that the suppression of certain interactions can be of benefit when designing spintronic devices. The low susceptibility and lack of stray fields could be used to create memory devices with a high resistance to external magnetic fields, and the THz response rates of moments to perturbations could present applications in high speed spintronics devices [14, 15].

Progress in the field of practical AFMs has however been reliant upon developing methods of changing and reading the AFM order, as most methods used in FMs are an even function of the sublattice magnetisation. One notable discovery is the ability for crystals with a broken inversion symmetry in their unit cell to experience relativistic current induced torque. Such relativistic torques are an even function of sublattice magnetisation and a such allow for efficient switching of AFMs [16, 17, 18]. In reading the AFM order, the anisotropic resistance of the sample can be used to differentiate between moments lying along different axes [19, 20, 21]. In 2016 these two effects were combined in a biaxial sample of CuMnAs to produce a memory resistor which can be both written to and read from electronically [18].

In order to further improve these devices more needs to be understood about the processes behind their operation. In this report we focus on two such issues. The first being to help in ascertaining values for A and Δ in CuMnAs. One way to investigate this is through measurements of the spin-flop transition. This transition is unique to AFMs and corresponds to the reorientation of the moments from the configuration shown in Figure 1a to that in Figure 1b. This occurs when a large enough magnetic field is applied along the anisotropic easy axis of the crystal. This rotation of moments can be seen by measuring the change to the anisotropic resistance (AR) in an AFM. As will be shown, spin flop occurs when $B = \sqrt{2\Delta A}$ in small samples.

Another approach utilises the dependence of domain wall width on A and Δ. A domain wall forms at the meeting of two magnetic domains, which consists of region of rotating magnetic order over some characteristic width. This width is predicted as $\delta_0 = M\sqrt{\frac{A}{\Delta}}$. X-ray magnetic linear dichroism photoemission electron microscopy (XMLD-PEEM) has previously been conducted on CuMnAs in samples of various thicknesses to image the domain structure at the surface [12, 18, 22, 23]. This has given an indication of the domain wall width in the material and provides an insight in to how it depends on the thickness of the CuMnAs film. The domain wall measurements also found variations present in the domain walls that makes acquiring a consistent value of the domain wall width a challenge. In order to understand the contributions to the variations in domain wall width, a model is produced in an attempt to generate some of the complex domain wall structures. Using the product of the domain wall width with the spin-flop field independent values for A and Δ can be found.

The second issue addressed in this report is the nature of the anisotropic signal, as it is currently assumed to be the result of anisotropic magneto-resistance (AMR). This is a phenomenon common in FMs that is an even function of the sublattice magnetisation [24], and should therefore be equally present in AFMs. This will be investigated through a comparison of zero field resistance measurements to those taken above the spin-flop field. We also consider the temperature dependent behaviour of the zero field signal, with our samples taken up to and above the Néel temperature which is the ordering temperature in AFMs. This allows us to check if the effect is dependent on the magnetic order of the sample or whether it is simply caused by material defects. Finally dynamic force microscopy (DFM) images were acquired of the sample in order to check for surface defects, hopefully to eliminate them as the cause of anisotropic resistance.

This report covers the necessary theory to understand the spin flop phenomenon and the origins of ARs, before describing the crystal structure and properties of tetragonal phase CuMnAs. The theory continues by explaining domain wall formation in AFMs and by explaining the basic principles of DFM. The theory is followed by an outline of experimental methods employed for spin flop and high temperature AR measurements. Next, the methods for simulating and detecting spin flop and for forming domain walls are outlined. This is followed by the results from each investigation and a discussion of the findings, including a crude estimate of the anisotropy and exchange strengths. This is concluded by a brief summary of the report and its discoveries.

Theory

In order to properly understand the methods and interpret the results of our project, several aspects of theory have to be discussed. The first is the origin of the spin-flop transition and a calculation for the spin-flop field in two limiting cases: a system containing only two moments and then one containing an infinite number of moments. Next is an description of the AMR effect and how it relates to the AFM order. The structure and known properties of CuMnAs are then described, to enable the creation of more accurate simulations and for the interpretation of the anisotropic resistance measurements. Penultimately, we discuss the theory behind domain wall formation in AFMs such that our domain wall models can be evaluated. Then a brief explanation of DFM is given.

Spin-Flop in Antiferromagnets

Spin-flop is a transition which takes place in response to a strong external magnetic field applied along the easy axis of an AFM such that the magnetic order switches from that shown in Figure 1a to that in Figure 1b, where the moments of each sublattice cant towards the applied field. This occurs where a field is above the spin-flop field since the energy penalty associated with the moments lying off the easy axis is less than the energy reduction associated with a net magnetisation developing in the AFM. The spin-flop field can then be calculated by finding the point at which the energies of the flopped and unflopped states are equal.

The energy of a moment, i, lying at an angle of θ_i to the easy axis of a one-dimensional crystal in a magnetic field, B, at an angle, ϕ, to the same axis is given by

$$E = -MB\cos(\theta_i - \phi) + 0.5AM^2\cos(\theta_i - \theta_{i-1}) + 0.5AM^2\cos(\theta_i - \theta_{i+1}) - 0.5\Delta\cos^2(\theta_i) \quad (3)$$

The parameters governing Equation 3 can be better defined as $B = u$, $AM = v$, $\Delta/M = w$ which allows a factor of M to be removed from Equation 3, and u, v, and w to be defined in units of Tesla. This allows for comparison between parameters and makes our results independent of M.

Spin-Flop for Two Moments

The energy of two moments in isolation is found by summing over Equation 3 for $i = 1$ and $i = 2$ whilst ignoring the terms which couple to any of the other moments. The energy of these two moments is then given by,

$$E_{2m} = -MB\cos(\theta_1 - \phi) - MB\cos(\theta_2 - \phi) + AM^2\cos(\theta_1 - \theta_2) - 0.5\Delta\cos^2(\theta_1) - 0.5\Delta\cos^2(\theta_2) \quad (4)$$

where θ_1 and θ_2 are the angles of moments 1 and 2 to the easy axis. When the system is in the unflopped state $\theta_1 = 0$ and $\theta_2 = 180°$. For the case where $B = 0$ Equation 4 becomes,

$$E_{2m} = -AM^2 - \Delta \quad (5)$$

For B above the spin flop field and with $\phi = 0$, the angle of the two moments to the easy axis must first be found in order to calculate E_{2m}. This can be done by solving for the two following differential equations:

$$\frac{\partial E_{2m}}{\partial \theta_1} = MB\sin(\theta_1) - AM^2\sin(\theta_1 - \theta_2) + \Delta\sin(\theta_1)\cos(\theta_1) = 0 \quad (6)$$

$$\frac{\partial E_{2m}}{\partial \theta_2} = MB\sin(\theta_2) + AM^2\sin(\theta_1 - \theta_2) + \Delta\sin(\theta_2)\cos(\theta_2) = 0 \quad (7)$$

which is done by summing over them both to give

$$MB(\sin(\theta_1) + \sin(\theta_2)) + \Delta(\sin(\theta_1)\cos(\theta_1) + \sin(\theta_2)\cos(\theta_2)) = 0 \tag{8}$$

Equation 8 is satisfied by $\theta_1 = -\theta_2$ in the flopped state. Rewriting Equation 6 with this relation and using the double angle formula for sine yields

$$MB\sin(\theta_1) - 2AM^2\sin(\theta_1)\cos(\theta_1) + \Delta\sin(\theta_1)\cos(\theta_1) = 0 \tag{9}$$

The factor of $\sin(\theta_1)$ can be ignored since its solution yields the unflopped solution, leaving

$$\cos(\theta_1) = \frac{MB}{2AM^2 - \Delta} \approx \frac{B}{2AM} \tag{10}$$

where we have assumed that the exchange term is much larger than the anisotropy term. In order to find the total energy of the flopped state, Equation 4 must be rewritten using $\theta_1 = -\theta_2$ and the double angle formula for cosine to give

$$E_{2m} = -2MB\cos(\theta_1) + AM^2[2\cos^2(\theta_1) - 1] - \Delta\cos^2(\theta_1) \tag{11}$$

Using Equation 10 the energy of the flopped state is now found to be

$$E_{2m} = -\frac{B^2}{A} + \frac{B^2}{2A} - AM^2 - \frac{\Delta B^2}{4A^2M^2} \tag{12}$$

$$E_{2m} = -\frac{2B^2AM^2 - \Delta B^2}{4A^2M^2} - AM^2 \tag{13}$$

Equating the energies of the flopped and unflopped states then provides the spin-flop condition

$$-AM^2 - \Delta = -\frac{2B^2AM^2 - \Delta B^2}{4A^2M^2} - AM^2 \tag{14}$$

$$B^2 = \frac{4A^2\Delta M^2}{2AM^2 - \Delta} \tag{15}$$

In the limit where $AM \gg \Delta/M$ this expression simplifies to

$$B_{\mathrm{sf}} = \sqrt{2A\Delta} \tag{16}$$

where B_{sf} is the spin-flop field. This value represents a lower limit for B_{sf} in a material as it considers the system in the limit where every moment experiences half the exchange interaction of an equivalent moment deep within the bulk, for a 1D system. This is due to its position at the surface.

Spin-Flop in the Bulk

The spin-flop field changes with the total number of moments in a system, and it is possible to calculate a value for B_{sf} in the bulk which represents the upper limit for B_{sf} in a material.

In calculating the spin-flop field in a bulk material we consider a general equation for the energy of moment i, which sums over N_s different interaction strengths of magnitude A_j with n_j neighbouring moments:

$$E_i = -MB\cos(\theta_i) + \sum_{j=1}^{N_s}\left[0.5n_jA_jM^2\cos(\theta_i - \theta_j)\right] - 0.5\Delta\cos^2(\theta_i) \tag{17}$$

In solving the energy equation in the bulk, a translational symmetry is assumed whereby the values of θ_i and θ_j are determined only by their respective sublattices. Each moment is assumed to only interact with those belonging to the other sublattice, and the moments of each sublattice experience the same number of interactions of the same strength as those in the other sublattice. With these assumptions the unflopped solution is $\theta_i = 0°$, $\theta_j = 180°$, and the flopped solution is $\theta_i = -\theta_j$. The sum of the energy of one moment from each sublattice is then given by

$$E_{2m} = -MB\left[\cos(\theta_i) + \cos(\theta_j)\right] + \sum_{j=1}^{N_s}\left[n_j A_j M^2 \cos(\theta_i - \theta_j)\right] - 0.5\Delta\left[\cos^2(\theta_i) + \cos^2(\theta_j)\right] \quad (18)$$

Solving Equation 18 in the unflopped state gives

$$E_{2m} = -\sum_{j=1}^{N_s}\left[n_j A_j M^2\right] - \Delta \quad (19)$$

In the flopped state the energy of the two moments is given by

$$E_{2m} = -2MB\cos(\theta_i) + M^2\sum_{j=1}^{N_s}\left[n_j A_j \cos(2\theta_i)\right] - \Delta\cos^2(\theta_i) \quad (20)$$

the solution to which can be found by solving

$$\frac{\partial E_{2m}}{\partial \theta_i} = 2MB\sin(\theta_i) - 2M^2\sum_{j=1}^{N_s}\left[n_j A_j \sin(2\theta_i)\right] + 2\Delta\sin(\theta_i)\cos(\theta_i) = 0 \quad (21)$$

which can be rewritten as

$$\frac{\partial E_{2m}}{\partial \theta_i} = 2MB\sin(\theta_i) - 4M^2\sum_{j=1}^{N_s}\left[n_j A_j \sin(\theta_i)\cos(\theta_i)\right] + 2\Delta\sin(\theta_i)\cos(\theta_i) = 0 \quad (22)$$

Here $\sin(\theta_i)$ can be ignored as it corresponds to solutions which lie along the easy axis. Equation 22 then reduces down to

$$\frac{\partial E_{2m}}{\partial \theta_i} = MB - 2M^2\sum_{j=1}^{N_s}\left[n_j A_j \cos(\theta_i)\right] + \Delta\cos(\theta_i) = 0 \quad (23)$$

$$\cos(\theta_i) = \frac{MB}{2M^2\sum_{j=1}^{N_s}\left[n_j A_j\right] - \Delta} \approx \frac{B}{2M\sum_{j=1}^{N_s}\left[n_j A_j\right]} \quad (24)$$

which can be substituted into Equation 20 to yield

$$E_{2m} = -\frac{B^2}{\sum_{j=1}^{N_s}\left[n_j A_j\right]} + M^2\sum_{j=1}^{N_s}\left[n_j A_j\left(2\left(\frac{B}{2M\sum_{j=1}^{N_s}\left[n_j A_j\right]}\right)^2 - 1\right)\right] - \Delta\left(\frac{B}{2M\sum_{j=1}^{N_s}\left[n_j A_j\right]}\right)^2 \quad (25)$$

Simplifying Equation 25 and ignoring the term in Δ, due to its typically small magnitude, gives

$$E_{2m} = -\frac{B^2}{2\sum_{j=1}^{N_s}\left[n_j A_j\right]} - \sum_{j=1}^{N_s}\left[n_j A_j M^2\right] \quad (26)$$

Equating Equation 26 and Equation 19 then provides the spin-flop condition,

$$\Delta = \frac{B_{\mathrm{sf}}^2}{2\sum_{j=1}^{N_s}\left[n_j A_j\right]} \quad (27)$$

and corresponding spin flop field

$$B_{\text{sf}} = \sqrt{2\Delta \sum_{j=1}^{N_s} [n_j A_j]} \tag{28}$$

In the one dimensional case, with $N_s = 1$ and $n_j = 2$, the spin flop field in the bulk becomes $B_{sf} = 2\sqrt{\Delta A}$. The difference between this field and that of the two isolated moments is the effect of the edge, as in the two moment case both moments behave as if they lie on the surface of the crystal, whereas in the bulk case none of the moments do. This would indicate that the spin-flop field increases as the number of moments n in the system increases.

Anisotropic Resistances

In a FM an anisotropic resistance (AR) varies as a function of the relative orientations of the current flowing through the material and the axis of the magnetic order. This is known as anisotropic magnetoresistance (AMR). In the single domain case the resistivity of a sample changes as [24]

$$\rho(\xi) = \rho_{\perp} \sin^2 \xi + \rho_{\parallel} \cos^2 \xi \tag{29}$$

where ξ is the angle between the current and the axis of the magnetic order, and $\rho_{\perp}$ and $\rho_{\parallel}$ are the resistivities when the current is perpendicular and parallel to the order respectively, typically $\rho_{\parallel} > \rho_{\perp}$. As AMR is an even function of sublattice magnetisation, it is expected that it should provide an efficient way of probing the AFM order.

Experiments in which the magnetic order of an AFM has been rotated by pinning to a FM layer indicate that the resistivity of an AFM material can vary as $\sin(2\xi)$, with an amplitude of 2% recorded in MnTe [20, 21]. Experimental results taken in CuMnAs indicate that this effect is in response to the magnetic order, as switching of a system by a current has been imaged using XMLD-PEEM and is shown to be the result of the switching of individual AFM domains [23, 8]

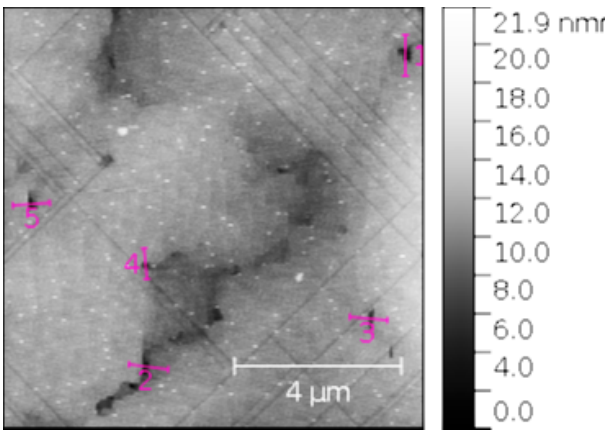

Figure 3: DFM image of a CuMnAs sample. The purple lines represent height profiles taken across cracks in the sample. Step edges in the crystal can also be seen in the long straight lines. Image courtesy of Reference [25].

Even though the form of the anisotropic resistance in these experiments matches that expected for AMR it is still not known if it is an AMR signal which is being measured. Other potential anisotropic contributions can be present in a sample, such a cracks which form as a result of lattice mismatch between the substrate and the sample material. Figure 3 shows cracks in a

sample of CuMnAs with the purple lines used to give profiles. The cracks had a typical measured depth of $\approx 10nm$ [25].

In addition to anisotropic contributions to the resistance signal there can also be isotropic ones. Using an L-bar as opposed to a single hall bar to take the resistance measurements cancels isotropic contributions as they will be symmetric between each arm of the sample, whereas the anisotropic terms should be antisymmetric. The isotropic contribution can be removed by taking the difference between the measurements.

Copper Manganese Arsenide

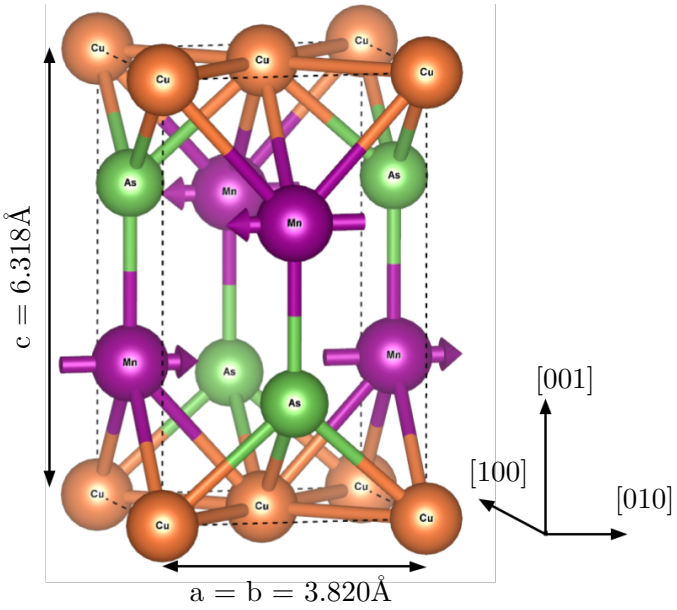

Figure 4: Unit cell for tetragonal CuMnAs. The purple arrows represent the anti-ferromagnetic coupling of the system. The layers in RC123 are stacked in the [001] crystallographic direction. The directions are the CuMnAs crystallographic directions not the substrate directions, which are also commonly used.

Tetragonal phase CuMnAs forms the unit cell shown in Figure 4. The manganese atoms are responsible for the magnetic properties of CuMnAs and in thick samples they have equivalent tendency to lie along either the [010] or [100] crystallographic directions. The arrows in Figure 4 show the moments lying along the [010] axis as is the case for thin samples, this is because the interface with GaP acts to break the symmetry of the system which induces uniaxial behaviour. The material's magnetic order, as with all antiferromagnetic materials, disappears at a characteristic temperature, known as the Néel temperature which has a value of 480 ± 5K in 500nm thick tetragonal CuMnAs [12].

A two dimensional (2D) model of CuMnAs is used for some of our domain wall simulations. In this model the structure shown in Figure 5a is used, with the coupling to nearest neighbours show by the purple lines. Here each moment interacts through the exchange interaction with four of its nearest neighbours. As shown, the coupling is only between vertically separated moments, and not between moments in the plane which belong to the same sublattice and therefore lie parallel to one another. For convenience, these layers will be referred to as FM planes for the remainder of the report, despite CuMnAs having a FM coupling strength of approximately zero. As illustrated, the FM planes are not equally separated with the spacings alternating between 2.1Åand 4.2Å, with the exchange coupling strengths alternating as $A_{\text{intra}} \approx 3A_{\text{inter}}$, for

interactions within and between the unit cell respectively [26].

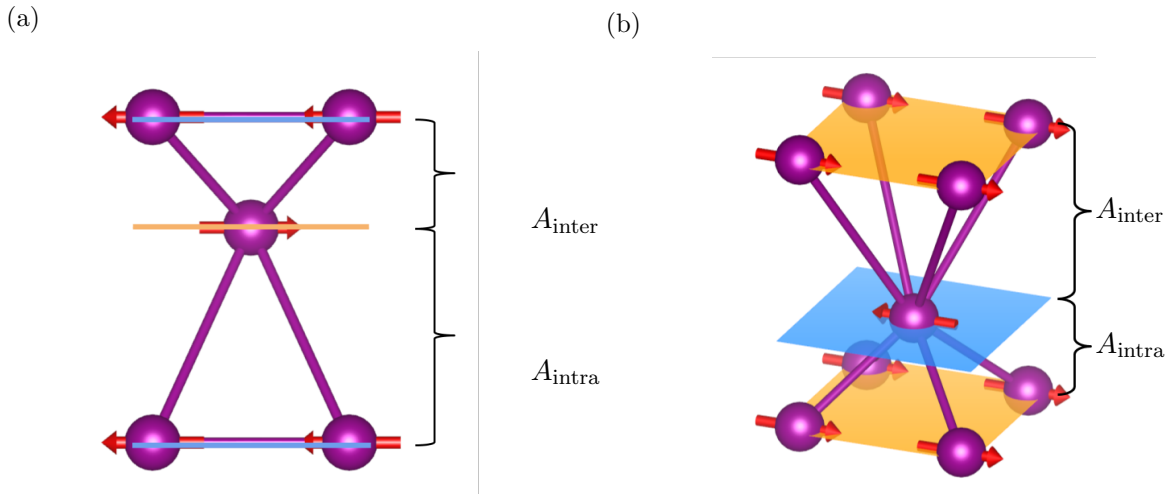

Figure 5: Ball and stick illustrations of the magnetic coupling of CuMnAs in the tetragonal phase. a) Shows the arrangement of magnetic coupling for each moment in the 2D simulations. b) Shows the magnetic coupling arrangement in 3D. The red vectors indicate the moment directions.

In 3D, each moment is coupled antiferromagnetically to eight nearest neighbours, with the system again forming FM planes, as shown in Figure 5b, with the same ratio of A_{intra} to A_{inter}.

In the 2D model, the spin-flop in the bulk is given by Equation 28 with $N_s = 2$, $n_1 = 2$, $n_2 = 2$, as

$$B_{\text{sf}} = 2\sqrt{\Delta(A_1 + A_2)} = 2\sqrt{2\Delta A_{\text{av}}} \tag{30}$$

In 3D, the values are the same but with $n_1 = 4$ and $n_2 = 4$, giving

$$B_{\text{sf}} = 2\sqrt{2\Delta(A_1 + A_2)} = 4\sqrt{\Delta A_{\text{av}}} \tag{31}$$

where A_{av} is the mean average of the two exchange constants.

Domain Wall Formation

In a FM material, a magnetic domain is a region of magnetism in which the moments are all aligned parallel to one another. In an antiferromagnetic material a domain is a region where moments align parallel within a sublattice and align anti-parallel between sublattices. When two domains are formed independently, and then meet, there is a high energy cost at the interface as a result of the exchange interaction, and a domain wall forms to allow one domain to smoothly transition into another. Along the profile of a domain wall, the moments gradually rotate to compensate for the sudden change in alignment and overall reduces the energy. In zero applied magnetic field, the width of the domain wall can be characterised by a zero field width factor $\delta_0 = \sqrt{\frac{v}{w}} \equiv M\sqrt{\frac{\Delta}{A}}$, which allows us to define the angle of a given moment as a function of its position, x, relative to the centre of the domain wall, x_0. δ_0 is a dimensionless quantity which represents the width. The angular variation for the moments in one sublattice along the profile of a domain wall in AFMs takes the following form [27, 28, 29]:

$$\theta = 2 \arctan\left(\pm \exp\left(\frac{x - x_0}{\delta_0}\right)\right) \tag{32}$$

but can also be represented as [30]

$$\theta = \arctan\left(\sinh\left(\frac{x - x_0}{\delta_0}\right)\right) \tag{33}$$

In a one dimensional domain wall, there are two equivalent solutions for the direction of rotation of the moments through the domain wall. This direction, or chirality, is referred to as either clockwise (for decreasing angle) or anti-clockwise (for increasing angle) and is why the exponent in Equation 32 can be either positive or negative.

In a 2D lattice, such as the FM case shown in Figure 6a, domain walls may be formed with different chirality along its length. These chiralities spread until they meet and form a pinched region referred to as a topological defect. Figure 6b shows the case for where the top row chose the clockwise chirality and the bottom row chose the anti-clockwise chirality leading to the formation of a topological defect in the centre of the lattice. Topological defects form in FMs and AFMs and can be detected using XMCD or XMLD PEEM techniques respectively. In both cases, the presence of a defect thins the domain walls and could influence domain wall motion, spin flop fields and various other magnetic properties.

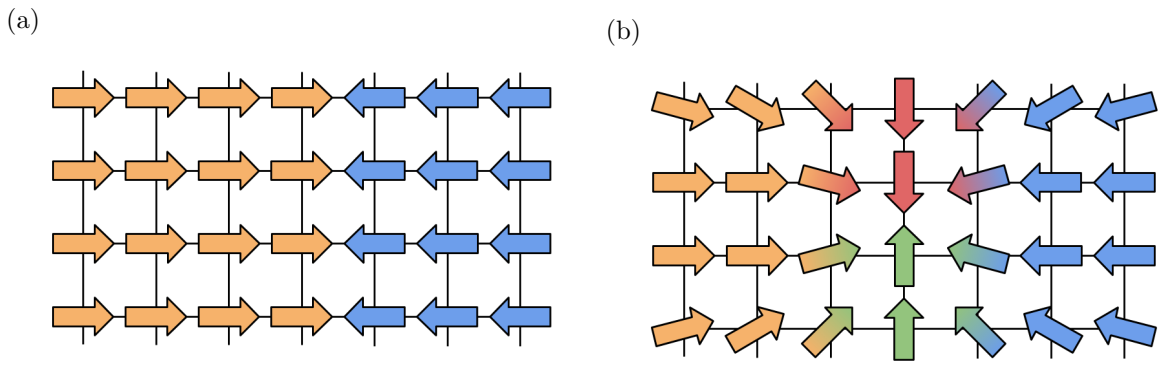

Figure 6: Schematic representation of the meeting of two ferromagnetic domains in two dimensions. a) Illustrates the form of the domains before the wall is formed to compensate for the high energy state. b) Shows the formation of a spontaneously formed topological defect which thins the domain wall.

In a FM material, the applied field will act to move the domain wall in the direction of the field which is a phenomenon utilised in racetrack memory and various investigations in storage and computation technologies [31]. An AFM domain wall, when a field is applied along an easy axis in order to induce a spin flop, the field will act to spread the domain wall until a flopped state is achieved. The opposite occurs along the hard axis. For antiferromagnetic chains in a constant field along the easy axis, the domain wall is predicted to change width according to

$$\delta_B = \delta_0 \sqrt{1 - B^2} \tag{34}$$

where δ_B is the characteristic width parameter in a field of magnitude B [30].

Dynamic Force Microscopy

Dynamic force microscopy (DFM), also known as non-contact atomic force microscopy, is a technique for imaging surface features with nanometre resolution. It is a form of atomic force microscopy and therefore has the same components. The device used consists of a sharp tip attached to the end of a flexible cantilever. A laser is shone at the tip of the cantilever and the

reflected signal is detected by a split photodiode, with the voltage generated by each region of the photodiode used to measure the deflection of the cantilever. The cantilever is driven with a piezoelectric material at a known frequency. The tip is set to oscillate and then brought close to the surface such that the tip interacts with the surface enough to affect the tip's resonant frequency. This is detected by the photodiode, alongside any change in amplitude and phase of oscillation, in order to determine the relative distance from the tip to the sample. The tip is scanned across a surface taking line profiles, which are then used to build up an image.

The DFM software used generates four images using different parameters: height retrace, amplitude retrace, phase retrace and z-sensor retrace. The height retrace is the most accurate measure of the height of surface features since, from the voltage applied across the piezoelectric material to maintain the setpoint, it estimates the difference in distance between the tip and points on the surface. The amplitude retrace is assembled from the magnitude of the signal in the feedback loop required to restore the setpoint. The phase retrace is an image of the difference in phase between the driving oscillation and the oscillation measured by the photodiode and the z-sensor retrace is formed from a measure of the position of the tip using a closed loop method. The z-sensor reading is effective for accurately measuring large features but does not detect features below 40nm accurately [32, 33].

Experimental Methods

This section details the experimental methods used to investigate two L-bar samples of a 20nm thick CuMnAS layer. We begin by describing the samples used, including a description as to how they were manufactured. We then continue to describe the experimental apparatus and methodology used in collecting the data in the four experiments we conducted: cryogenic field sweeps, alignment investigations, high temperature resistance measurements, and DFM imaging of a sample off-cut.

Samples RC123 L1 and RC123 L2

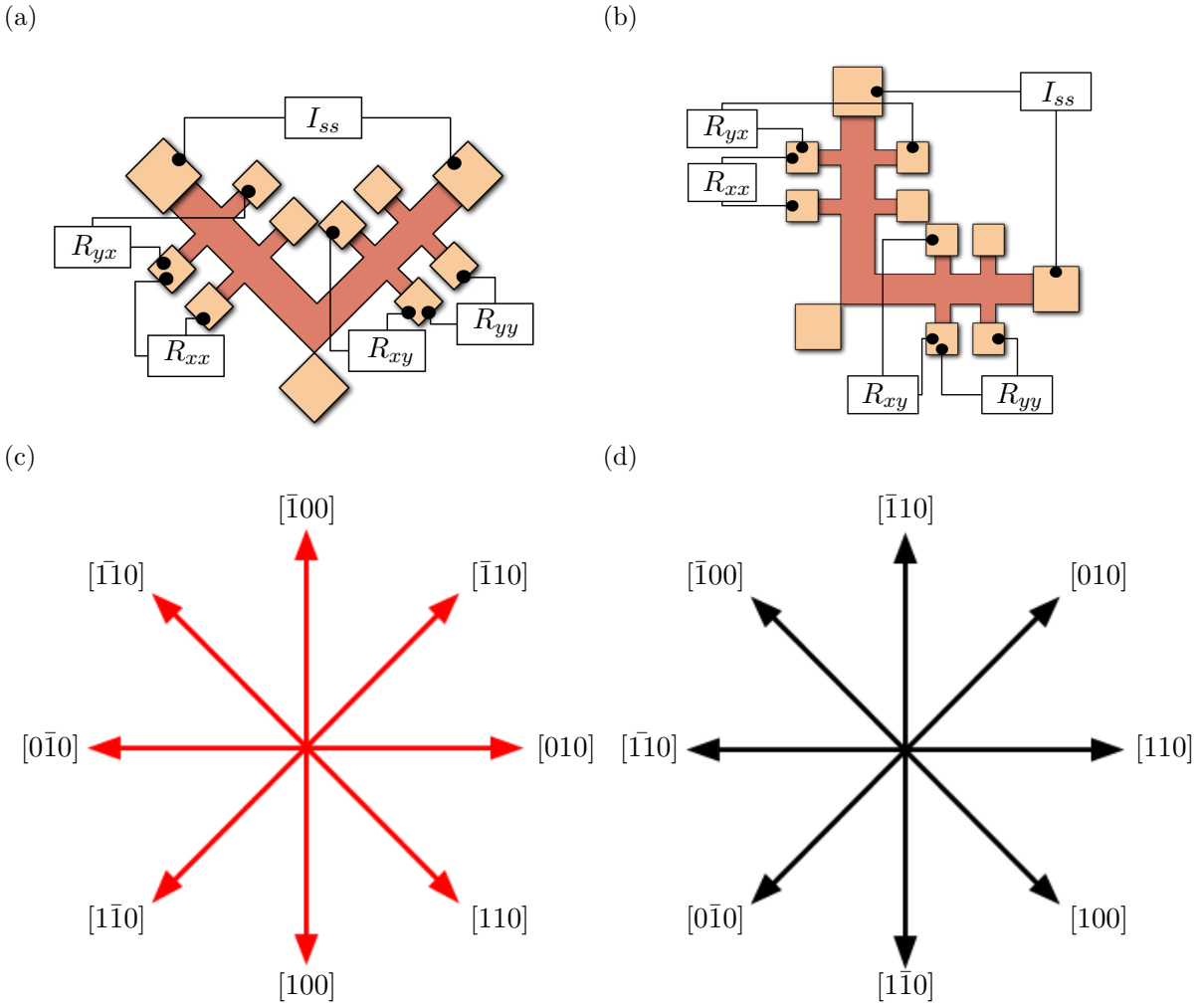

Figure 7: Schematic diagrams of a) sample L1 and b) sample L2. In both samples the x direction is defined as the direction of current in the first arm. All measurements use the measurement at the shared contact as the positive voltage. c) Shows the crystallographic directions in CuMnAs for both samples while d) the crystallographic directions of the GaP substrate for both samples.

A 20nm CuMnAs layer named RC123 was grown in the tetragonal phase atop a GaP substrate using molecular beam epitaxy by Campion, R. et al with a methodology similar to those employed in in References [12] and [34]. The exposed CuMnAs surface of RC123 was then capped with an Al layer to protect the sample from oxidation. The 20nm thickness corresponds to approximately 32 unit cells, resulting in a sample which is approximately 64 magnetic moments thick. The wafer

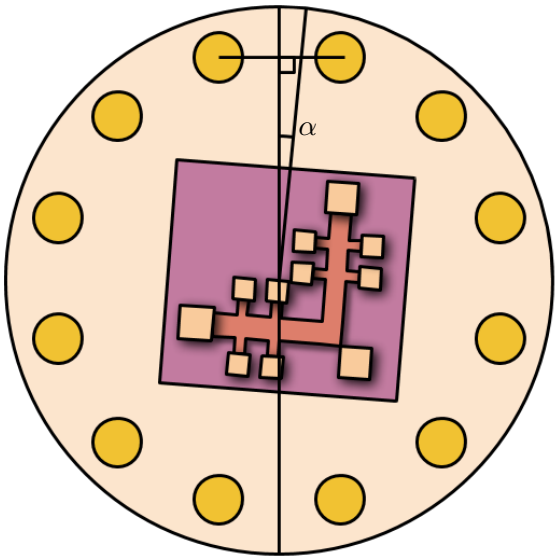

Figure 8: Schematic diagram of a sample mounted on its holder. The angle α represents misalignment between the samples crystallographic axes and the pins on the holder.

was imaged using XMLD-PEEM and found to be magnetically uniaxial in the [010] CuMnAs direction [22]. Two pieces were cut from the wafer upon which L-shaped hall bars were etched using photolithography techniques by Wang, M. One of the samples, L1, had arms etched at 45° and 135° to the easy axis, as shown in Figure 7a. L2 had arms etched at 0 and 90° to the easy axis as shown in Figure 7b. This allowed for $R_{\parallel}$ and $R_{\perp}$ to be measured along four major crystallographic axes. The distance between the contacts used for measuring R_{yy} as well as the contacts used for measuring R_{xx} on both samples was 200µm, and the separation between the contacts used to measure R_{xy} and those for R_{yx} was 100µm for both samples.

The samples were fixed to separate sample holders using an adhesive, and wires were bonded between the contacts on the sample and the pins on the holder. The resulting samples in their holders are like that schematically shown in Figure 8. Samples L1 and L2 were used in this arrangement for all experimental results, except the DFM image which used a small off-cut from the larger RC123 sample.

The current was always passed in the same direction between the contacts labelled with I_{ss} in Figure 7, and the x and y axes were defined as the axis of the first arm and second arm respectively. When measuring the four wire resistances for R_{xy} and R_{yx} the contact on the outside of the bend in the sample was used for measuring the positive contact voltage.

Images of the surface domain structure of RC123 were taken by a group from the University of Nottingham at Diamond Light Source, Oxford using XMLD-PEEM. Two such images are shown in Figure 9, with the brightness of the pixels corresponding to the angle of the magnetic order relative to some axis. Due to the nature of AFMs there is no difference between separate domains, but the domain walls can be seen as the dark lines in the images. The images show two different regions containing domain walls. These were analysed by others, but showed that the domain wall is approximately 0.1±0.05µm wide which corresponds to ≈ 300 unit cells [22].

(a) (b)

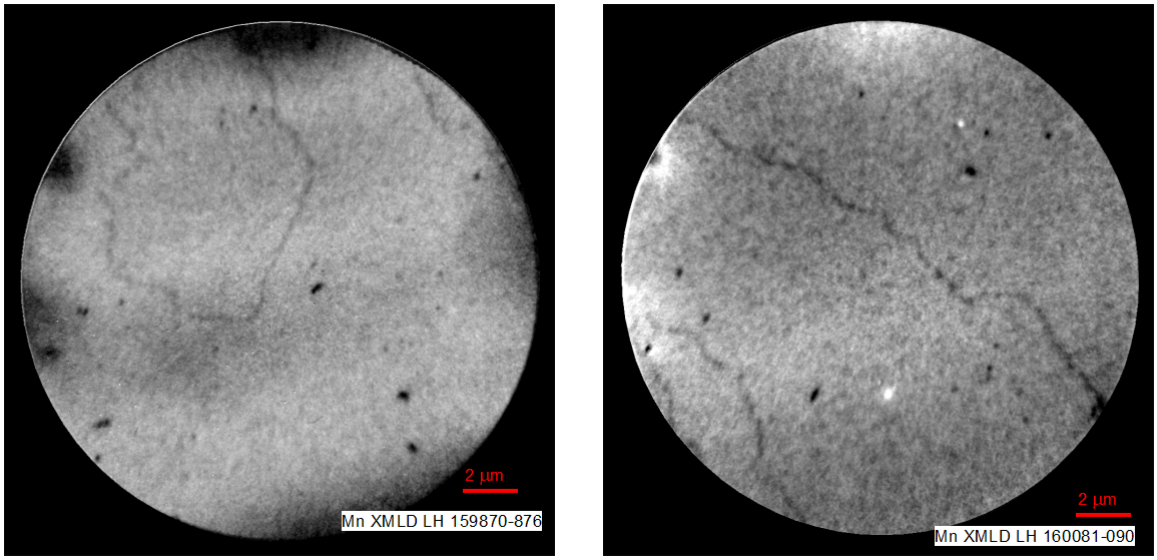

Figure 9: XMLD-PEEM images of RC123 acquired at Diamond Light Source by Wadley, P., Edmonds, K. and Reimers, S. [22]. The scale bars show the size of 2µm on the image, with each pixel having an area of 10nm×10nm. The light regions contain moments aligned along the easy axis where the darker regions contain moments aligned along the hard axis at 90° to the easy axis.

Spin-Flop Measurements

Our samples were placed in a cryogenic chamber surrounded by a superconducting solenoid submersed in liquid helium, as illustrated in Figure 10. The sample space was cooled by opening a needle valve in the base of the chamber, with fine temperature control provided by a PID controlled heater which heats the helium as it passes through the valve. A thermocouple positioned near the needle valve provided the feedback to the PID controller and provided temperature information.

In order to detect a spin-flop we recorded the anisotropic resistances of our samples. In each sample two 4-wire resistance measurements were taken, parallel to and perpendicular to, the direction of the current. The values for both the parallel and perpendicular resistance were recorded for both arms such that the isotropic contribution could be removed by taking the difference. The relative anisotropic resistance measurements were calculated using

$$\Delta R_{\parallel} = \frac{R_{xx} - R_{yy}}{R_{xx} + R_{yy}} \tag{35}$$

$$\Delta R_{\perp} = \frac{2(R_{yx} - R_{xy})}{R_{xx} + R_{yy}} \tag{36}$$

where R_{xy}, R_{yx}, R_{xx} and R_{yy} are those defined in Figure 7. The factor of two in calculating $\Delta R_{\perp}$ is to compensate for the shape of our sample. The denominators in the anisotropic resistance expressions act to normalise the values.

When recording a field sweep, the superconducting magnet controller output the field strength to a computer for recording purposes. The multimeters used to make the resistance measurements were triggered simultaneously using computer control and then values were read off sequentially

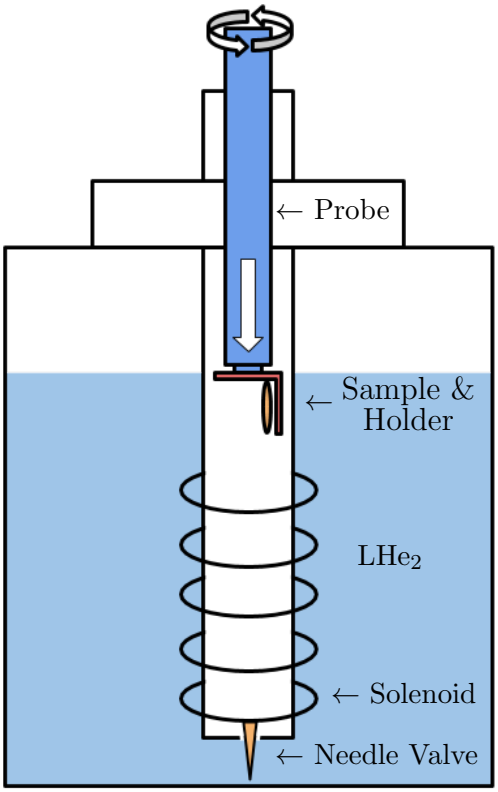

Figure 10: Schematic diagram of a superconducting magnet in a liquid He cryostat with sample and probe shown. The needle valve at the bottom of the sample chamber allows He to flow to cool the sample and a heating element placed near the inlet heats the He in order to control the sample temperature. The probe shaft was rotated inside the coil to check that the solenoid was in-line with the axis of the probe shaft.

after each trigger event, with the field strength recorded at the same time. This was done to minimise the effect of thermal noise on our data. Plots of the AR signals were made against the field applied to look for the spin-flop transition. The spin-flop transition should be a well defined step in the AR signal with smoothed edges as a result of any misalignment between the field and the easy axis. The spin-flop field can be found by fitting a Gaussian to the spin-flop plot with the full width half maximum (FWHM) used to find the spin-flop field.

Currents of 0.5mA and 1.0mA were typically used in these experiments. The sweeps rose to either $\pm$4T or $\pm$7T and all field sweep measurements were conducted at 2.5K except for one at 150K, which was done to observe any decay of the spin flop amplitude with temperature. The variation in the measured temperature at 2.5K was kept within 5mK.

Alignment Investigations

There are several factors which could reduce the sharpness of the spin flop transition or reduce the signal strength. Misalignment between the applied field and the easy axis of the sample would reduce the sharpness of the flop signal, and so two investigations were conducted to investigate sample alignment. First the sample holder probe was rotated inside the solenoid, as shown by the arrows at the top of Figure 10. This allows us to check the alignment of the solenoid. The second alignment investigation rotates the sample holder between pins. This rotation could be achieved using two separate adaptors to allow rotations in steps of 15°. This

allowed us to confirm the angle, α, shown in Figure 8 to within 7.5°. The alignment for both sets of rotations was checked by performing spin-flop sweeps and comparing the amplitudes.

High Temperature Measurements

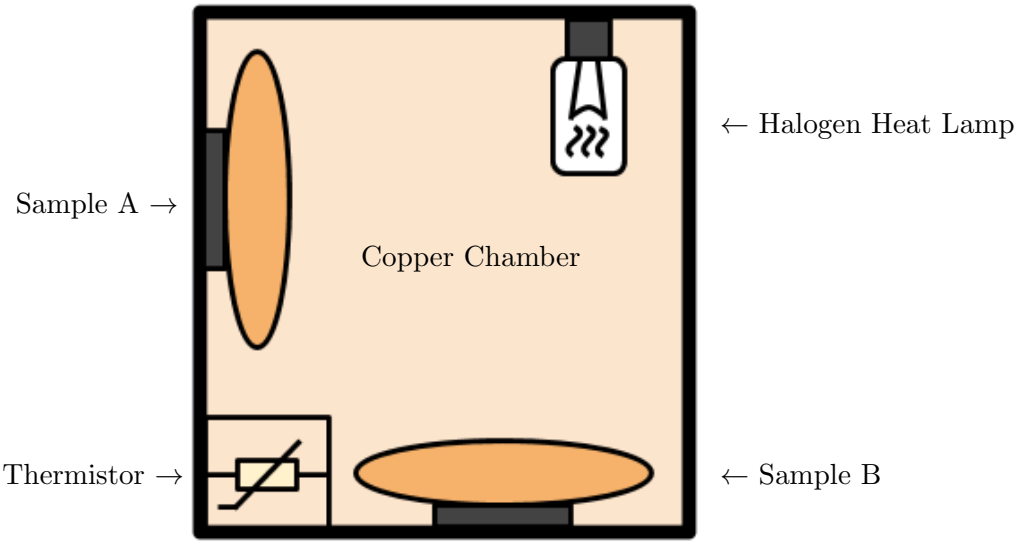

Figure 11: Schematic diagram of the high temperature copper chamber which was submerged into ultra high vacuum for use in the high temperature resistance measurements.

In order to observe the change in the anisotropic resistance with temperature, we had to use two sets of apparatus, the cryostat for 2.5K-300K and a high temperature rig for 300K-500K. The data collected in the cryostat used the same triggering methodology as for the spin-flop measurements, with the temperature fluctuations allowed to settle to less than 1K before data was then recorded for two minutes, with the average used to provide the AR signal.

For the readings taken above 300K the equipment shown in Figure 11 was used. This consisted of a copper cylinder with two sample holders and a halogen heat lamp. This sample chamber was loaded into a vacuum chamber and maintained at a pressure of between 10^{-6}Torr and 10^{-8}Torr. This provided a very stable temperature and inhibited oxidation of the samples. The halogen lamp heated the chamber with the surrounding copper acting as a passive radiator. Using a PID controller for the heat lamp power then allowed for thermal control of the sample space. For each sample, the AR measurements were made as with the cryogenic system, however because a switch box was used to make the readings, a slight delay exists between each measurement.

In the high temperature system, multiple sweeps were recorded with multiple runs between 300K and 440K, before the samples were then taken up to 500K multiple times, at rate of $\sim$ 1K/min. Between each sweep, the sample space was left to passively cool back down to 300K before the next data set was recorded. If the only contributor to anisotropic resistance is magnetic in origin, raising the sample close to or above the Néel temperature should reduce the signal to zero. By plotting the AR signals against temperature, it could then be seen if the anisotropy disappeared at the Néel temperature.

Dynamic Force Microscopy Imaging

Cracks and other surface defects can contribute to the AR signal, especially if cracks lie along a crystallographic direction. In order to test for such defects, DFM was performed on a small off-cut of RC123. Of the four images generated by a DFM scan, the height and amplitude images are most useful. The height map and line profiles are used tune the setpoint voltage since differences in the line profile for traces in opposite directions indicate a setpoint that is either too low or too high. The amplitude trace indicates the position and shape of defects very well and with low noise, although the heights indicated by the amplitude and phase retraces do not represent real space heights.

In order to acquire the surface images, the sample was washed in acetone and placed in the sample space under the probe. The laser was aligned with the reflective region of the DFM cantilever to maximise the signal. At this point, a calibration was performed to determine the resonant frequency and other parameters of the cantilever away from the sample. The tip is brought in close to the sample and the integral gain was was set to 10. A preliminary scan was performed in order to find a good setpoint current for the photodiode. The set point was initially set to 800mV and reduced in steps of 25mV until the height line profiles for forward and backward were as similar as possible. This setpoint was used for each scan at that size, and was found again every time the scan size was changed. Scans of the GaP surface and the Al capping layer were taken at multiple locations on the surface, with different scan sizes ranging from 100nm x 100nm to 20µm x 20µm. The resulting height retraces and amplitude retraces were then opened in an image processing program to remove any gradients present, scars were removed and the colour map was adjusted to fit the desired range of heights well.

Simulations

Various interesting phenomena can be simulated using a simple energy expression for the moments in an AFM lattice. The simulations branched into two primary aims, the first being to determine the spin flop field of a given system, and then to determine the effects of surfaces on spin flop, these investigations were primarily conducted in one-dimension. The second branch aimed to investigate the factors which control the width of domain walls in CuMnAs, with investigation in both two and three dimensions.

Both branches used the same model to find the steady state solution. This model worked by finding the local energy minimum for a given initial condition, with the energy of each moment as given by Equation 17. By introducing a virtual time, the rate of change in the angle of each moment relative to the easy axis can be written as

$$\dot{\theta}_i \propto -\frac{\partial \sum_i E_i}{\partial \theta_i} \tag{37}$$

Solving Equation 37 when $\dot{\theta}_i = 0$ for all the moments in the system yields a local solution to Equation 17. A solution to Equation 37 can be found using an ODE solver, where increasing virtual time allows a more accurate solution to be found. Putting Equation 17 into Equation 37 yields the explicit form for the equations we used to find our solutions

$$\dot{\theta}_i = -MB\sin(\theta_i) + \sum_{j=1}^{N_s} \left[n_j A_j M^2 \sin(\theta_i - \theta_j)\right] - \Delta\cos(\theta_i)\sin(\theta_i), \tag{38}$$

where the constant of proportionality in Equation 37 has been set to unity. As the system finds local minima both flopped and unflopped initial conditions must be considered with the energy of the final states compared in order to find out which is the global minimum. Both initial conditions have a small random offset to prevent the system becoming stuck a potential maximum. In addition to the energy comparison, the relative orientations of the moments in the final state are checked to ensure that neither of the two states has finished in that of the other state, as can happen when the field is far away from the spin-flop field.

Spin Flop Simulation Approach

When determining the the spin-flop field from the simulation, an external magnetic field is applied along the easy axis with a strength below the expected spin-flop field by $0.2 - 1T$. The steady state solutions from the flopped and unflopped initial conditions are then found and their energies are compared. This process is repeated with strength of the field increased each time until the energy of the flopped state is less than that of the unflopped state, at which point the spin-flop field is said to have been reached.

The length of virtual time, t, allowed for the simulation to find the stationary solutions must be large because, by definition, the energies of the two states are very similar near the spin-flop field. With $M = 1$ and the constant of proportionality in Equation 37 set to one, we used a range of $t = 2000 - 20000$ depending on the circumstances when making spin-flop measurements. These values of t were arrived at by increasing t until the results became consistent. The situations which require a large t are: systems with a larger number of moments, systems for which B_{sf} changes rapidly with number of moments, wrapped systems, and systems with a larger number of dimensions. The value of t used will also influence the values used for the field steps and its initial value for B, as increased accuracy from both results in greater computational time.

In determining how B_{sf} varies with the total number of moments in the crystal, the system starts with a small n and calculates the spin-flop field, once this is done the size of the system is increased and the process repeated. In order to save time whilst running these simulations the B_{sf} for the previous number of moments was used, minus some value, as B_{sf} should increase with n, if n is even.

Domain Wall Simulation Approach

Domain walls were simulated in one, two, and three dimensions all with similar parameters and approaches. The initial conditions were set as two domains meeting at the centre of the system, before solving for the steady state solution. In dimensions above one, the formation of topological defects was observed. In order to eliminate these defects, the chirality of the domain walls could be made uniform by changing the initial conditions. Specifically, the middle moments in each sublattice were set to 90° and 270°. If defects were preferable, increasing the size of the random offset for the moments increased the chance of topological defects forming.

The domain wall simulations were performed with the intention of determining how their widths grow under increasing applied field, and to compare them with analytical predictions. The simulation could then be used to investigate the extent of domain wall thinning caused by topological defects and what effect having two different coupling strengths plays on domain wall width. For the applied field investigations a one dimensional model was used. For the other investigations a two dimensional model was used, however a working three dimensional model was made. The three dimensional model was too slow to be used for any systematic investigations.

In order to determine the extent to which the applied field widens the domain wall, a one dimensional antiferromagnetic chain was made to be half the length of the system. Another one dimensional chain with a 180° difference in phase was made and used for the second half of the system. This produced an antiferromagnetic domain wall in 1D where the two halved meet. The model was allowed to evolve using the approach described above with $t = 2000$ and $B = 0\text{T}$. The resulting domain wall was then fit to an analytical solution of the form given in Equation 32. In order to avoid having to fit twice, once with positive and once with negative exponential, the middle moment was set to π thus forming an anti-clockwise domain wall. This one dimensional model was then run with fields applied along the easy axis with values of -1.8T to 2.0T in steps of 0.1T. The the resulting value of δ_B was recorded after each simulation.

To investigate the effect of topological defects on domain wall width, a two dimensional model representing the coupling illustrated in Figure 5a was made. This contained rows of parallel moments in one dimension separated by rows of parallel moments in the opposite direction. This allowed the formation of a domain wall in the FM plane of the crystal, similar that in Figure 6a. Each moment had a random offset applied to it in order to increase the chance of defect formation and contour plots of constant angle were used to illustrate the width of the domain wall.

To investigate the effect of a two-valued coupling strength, the initial conditions were tweaked to give a single chirality across the entire domain wall. The domain wall width for each sublattice was found using the same method as in the one dimensional case and the free fit parameter was rearranged to give

$$\delta_B = M\sqrt{\frac{\Delta}{A_{\text{fit}}}} \implies A_{\text{fit}} = \frac{M^2\Delta}{\delta_B^2} \tag{39}$$

where A_{fit} is the effective coupling strength if Δ remains unchanged. This allowed the effective coupling strength to be determined from the domain wall width.

Results

In this section we present some of the key experimental results that were obtained over the course of this project, the majority of which are for sample L1 as it exhibited the larger anisotropic signal. The section starts with a description of the experimental results with the data pertaining to spin-flop measurements, at 2.5K, being used to make a determination for the spin-flop field. Sample rotations are presented to confirm the uniaxial nature of the sample. We then go on to present the results relating to he changing AR signal with increasing temperature, with spin-flop measurements at 150K also given. The final experimental section presents the data from the DFM imagining we conducted on a off-cut of RC123.

Spin Flop and Alignment Results

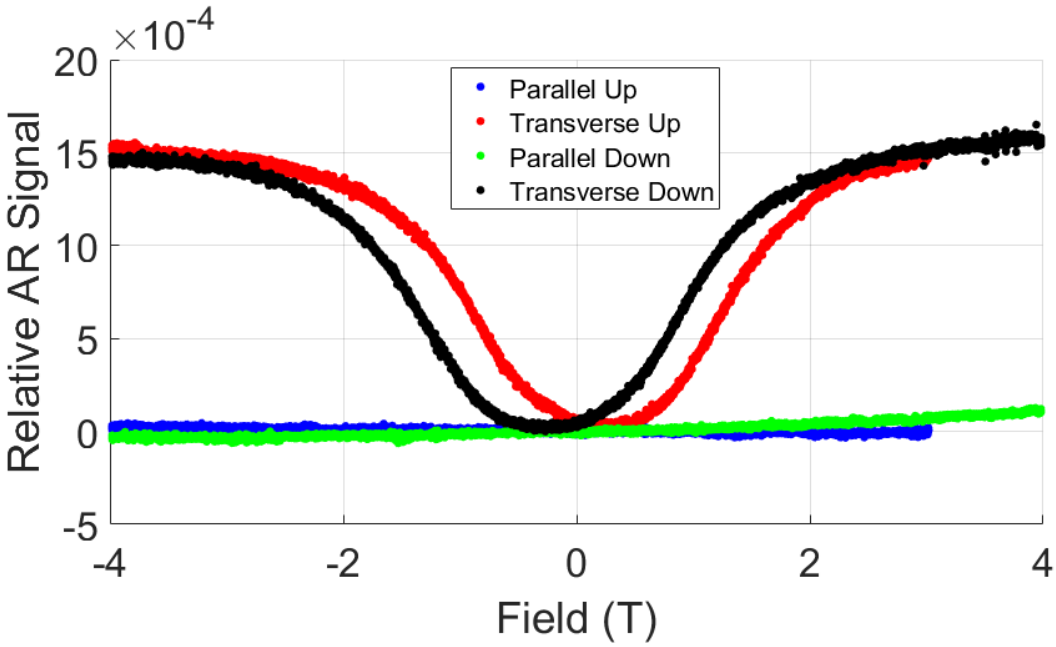

Figure 12: Plot of the AR signals for L1 under a field sweep with increasing and then with decreasing field in order to observe hysteresis. Field applied along the [010] crystallographic direction at 2.5K

Samples L1 and L2 were placed in the cryostat and a magnetic field was swept between -4T and 4T along the [010] crystallographic axis. A plot of two such sweeps is shown in Figure 12 with the two offset flop profiles being the result of the direction in which the field is swept. The parallel AR signal exhibits no variation with B, whilst the transverse signal exhibits a characteristic spin-flop profile as would be expected in L1. By fitting a Gaussian profile to the transverse signal the spin-flop field can be extracted from the FWHM, by doing this for three field sweeps on L1 the spin-flop field has been calculated as $B_{\text{sf}} = 1.48 \pm 0.04$T. The amplitude of the spin-flop was also found from the Gaussian fit to be $(1.54 \pm 0.03) \times 10^{-3}$. L2 exhibits the same characteristics as L1 albeit with the forms for the parallel and transverse resistances reversed. By fitting a Gaussian to the L2 data the value for the spin-flop field is found to be $B_{\text{sf}} = 1.44 \pm 0.07$T and the spin-flop amplitude is $(1.20 \pm 0.05) \times 10^{-3}$. The amplitude of the L2 signal was therefore 78±3% that of the L1 signal.

In order to check for any other anisotropic easy axes, a field sweep was conducted along the [010], [110] and [100] CuMnAs directions corresponding to 0°, 45° and 90° respectively in Figure

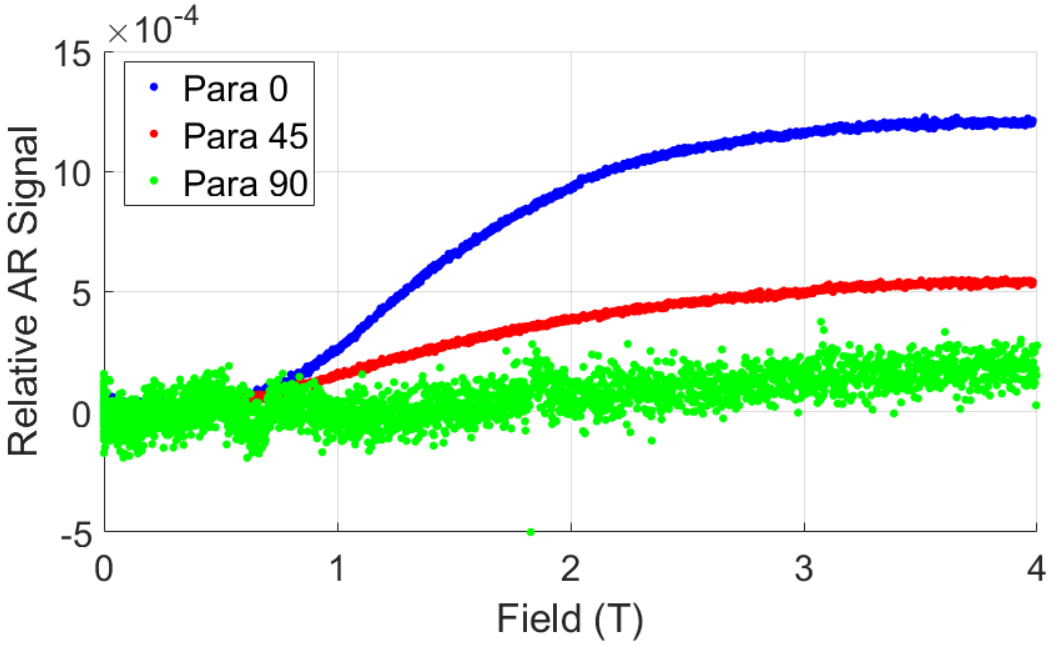

Figure 13: Field sweeps from 0 to 4T were conducted on sample L2 along three axes at angles 0°, 90° and 180° to the [010] easy axis at 2.5K. Spin flop occurs for 0 and 45 but not for 90.

13. The AR signal is approximately 1.2×10^{-3} at 0°, 0.6×10^{-3} at 45° and 0.2×10^{-3}. The expected AR signal ratio between maximum signal at 45° to the easy axis is

$$sin^2(45°) = 0.5 \tag{40}$$

and so it is clear to see that the [010] direction is the easy axis in our sample.

(a) (b)

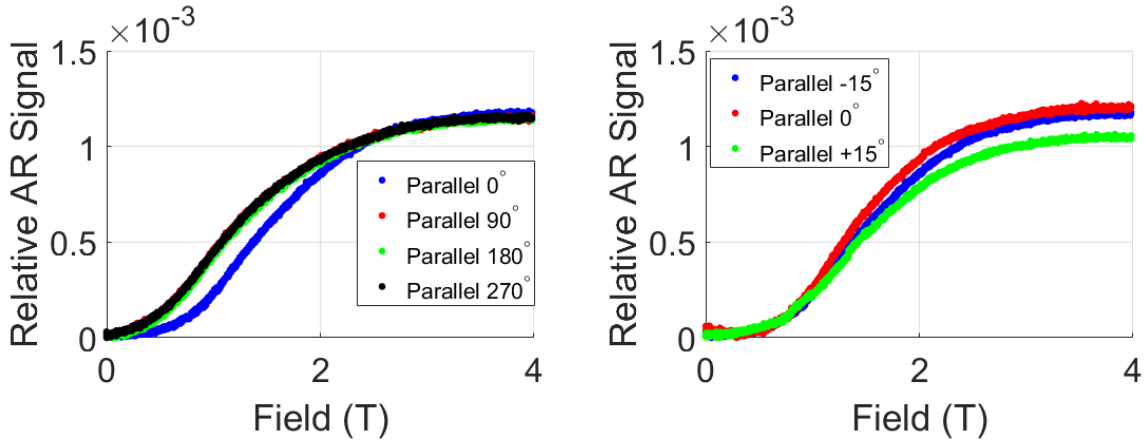

Figure 14: Alignment check results where sweeps from 0 to 4T were conducted. (a) shows data for L2 where the whole probe was rotated in the axis of the solenoid. (b) shows the data where the sample was mounted in three pin locations: the original (0°) and at a rotation of -15° and +15°.

Sample L2 was placed into the cryostat with the easy axis rotated in the sample holder by -15° and 15° to the original direction (0°). Figure 14b shows the parallel AR signals for the three sweeps for different alignments. The amplitude of the signals can be identified as lowest at 15°.

The data suggests that the maximum value lies between 0° and -15° and lies closer to 0°. We conclude from this the value of α must be between 0° and -7.5°. Even if this is at a maximum offset of -7.5° the value of $\cos^2(7.5) = 0.98$, which is too small to account for the different flop amplitudes between L1 and L2 and therefore suggests the difference between L1 and L2 is not an alignment issue.

Sample L2 was placed in the sample holder on the pins corresponding to +15°. Four sweeps were then conducted with a 90° rotation of the sample in the probe being applied. The resulting parallel AR signals are plotted in Figure 14a. From this it can be seen that the first sweep results in a slightly higher spin-flop field however it reaches the same maximum value as the others. The other three lines are identical indicating that the alignment was not causing the difference in the 0° data.

Temperature Variation Results

The first part of the investigation into the AR signal was to take spin-flop measurements at 150K such that the amplitude could be compared to those at 2.5K, this was done using sample L1 as it showed the larger spin-flop amplitude at 2.5K. The results for field sweeps in L1 between -4T and 4T along the [010] crystallographic direction are shown in Figure 15. At both temperatures an

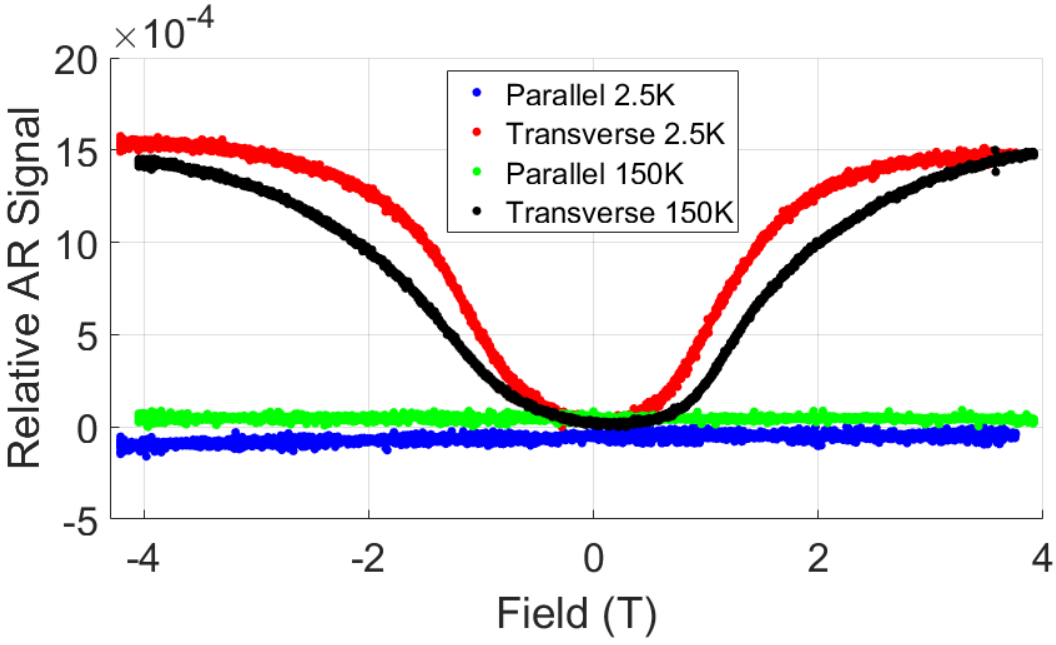

Figure 15: Plot of the AR signals for L1 in sweeps for an applied field -4 and 4T along the [010] easy axis. The blue and red lines show the data from a sweep at 2.5K while the green and black lines are for a sweep at 150K.

offset has been applied to the B axis in order to centre them both at 0T. The spin-flop transition is noticeably softer at 150K than at 2.5K and the trace still shows a significant curvature at 4T. The spin-flop field is also changed at 150K and was found to be 1.9 ± 1T. The amplitude of the spin-flop signal remains very similar to that at 2.5K at a value of $(1.4 \pm 0.1) \times 10^{-4}$.

The second part of of the investigation into the AR signal was to observe how it and its constituent components varied with increasing temperature up to and above the Néel temperature. The data from 2.5k to 200k was recorded in the cryostat, the data recorded at 300K was obtained with the samples stationed within the same sample holder but in an open air environment. The data

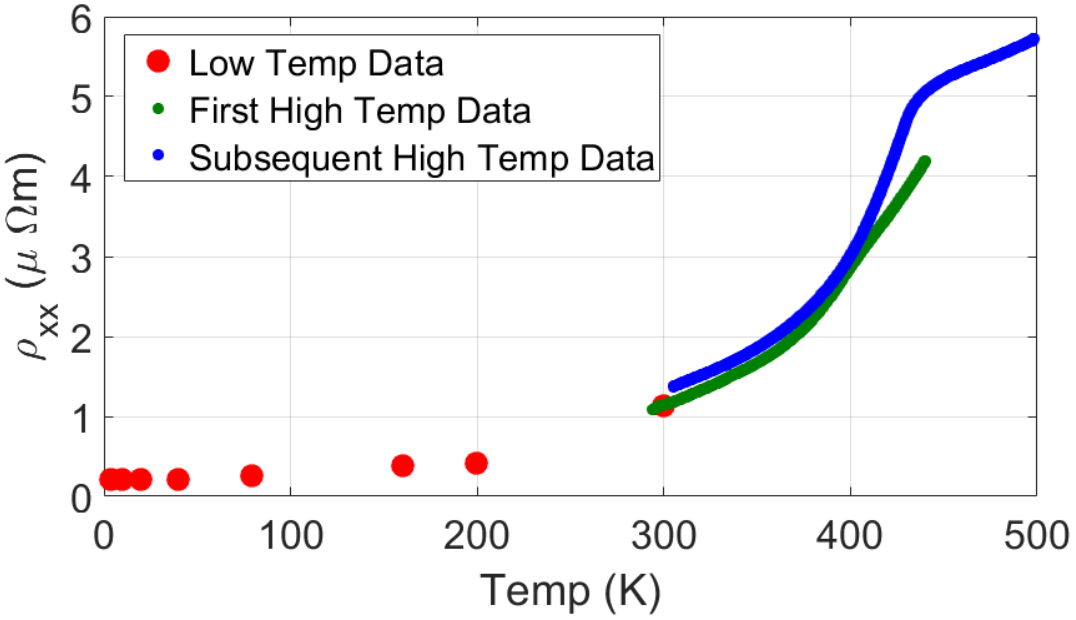

Figure 16: Plot of how the resistivity in L1 changes with temperature over the range 2.5K to 500K.

sets recorded between 300k and 500k were all taken in the high temperature rig. The nature of the high temperature rig is such that both samples must be heated and cooled together, and equipment limitations meant we could only record the AR signal for one sample at a time. We chose to focus on sample L1 as it had the larger signal at 2.5k to 300k. This meant that it was chosen for our first sweep up to both 440K and 500K. The data for L2 was recorded up to 440K before the first 500K sweep and then the 500K L2 data was recorded after the first 500K sweep.

In all the plots showing the temperature variation of the AR signal and its components: the red dots represent data collected in the cryostat or cryostat holder for L1, with the equivalent L2 data represented by orange dots; the green line represents L1 data for the first time the samples were taken to 440K; the dark blue line shows the L1 data for the first time the samples were taken to 500K; the purple line represents the L1 data for the second time the samples were taken to 500K; and the light blue line is data for L2 taken up to 440K before it was taken up to 500K. In finding the uncertainty for the temperature variation data, the difference between the measured temperature and the sample temperature is the biggest source of error. The temperature vaiation in the cryostat was a maximum of $\pm$1K and in the high temperature rig it was no more than $\pm$5K as a result of thermal lag. The uncertainty is then calculated by considering the signal variation across this range as an indicator for uncertainty. In some cases the error is smaller than the precision of the given value, in which case the error given is that of the precision of the presented result.

Figure 16 shows the variation in ρ_{xx} for L1 over the range 2.5K to 500K. We found good agreement between ρ_{xx} and ρ_{yy} at all temperatures as would be expected in L1. Here, ρ_{xx} increases from a value of $0.21 \pm 0.01\mu\Omega$m at 2.5K to $5.73 \pm 0.03\mu\Omega$m at 498K. Where the red and green data sets meet at 300k the values are $1.13 \pm 0.01\mu\Omega$m and $1.14 \pm 0.04\mu\Omega$m respectively. The difference between the dark blue and green lines is the result of the sample spending > 5 hours at 440K. This created a difference of $0.19 \pm 0.06\mu\Omega$m at 305K and a difference of $0.9 \pm 0.2\mu\Omega$ at 440K. Finally a kink can be noted in the dark blue trace in Figure 16 which could be indicative of the sample reaching the Néel temperature, the position of the kink has

been found as 440 ± 10K by differentiating the blue curve twice with respect to temperature and then finding the minimum.

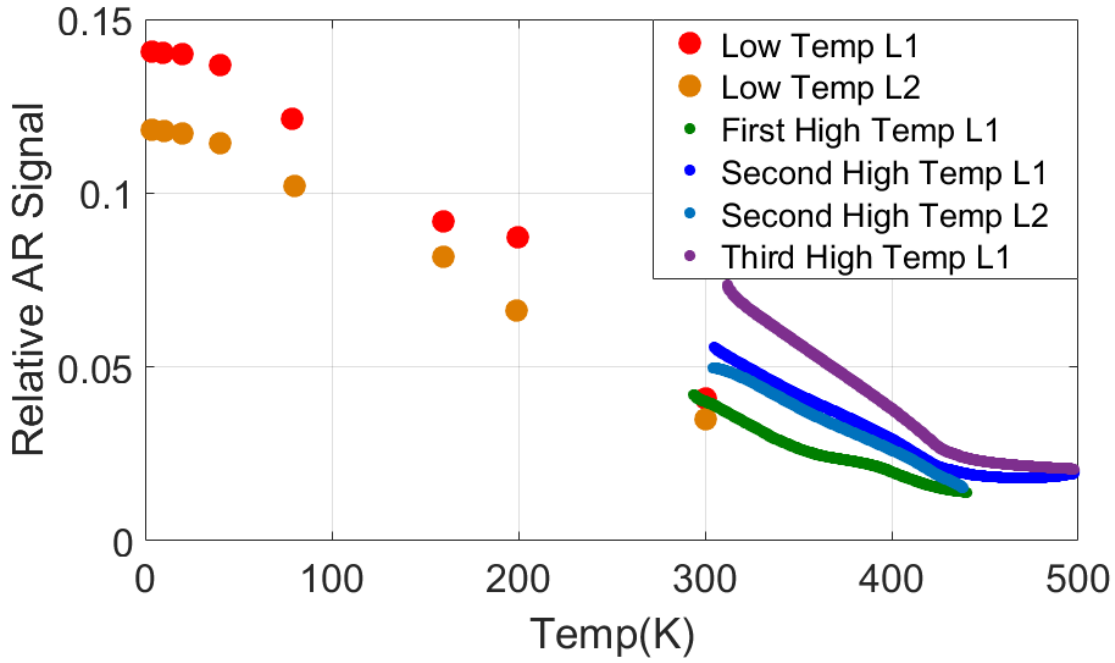

Figure 17: Plot for how the measured relative AR in L1 and L2 changes of the the temperature range 2.5K to 500K.

Figure 17 shows how the relative AR signal varied in L1 and L2 over the range 2.5k to 500k. Qualitatively the data shows a clear downward trend with a small plateau between ≈ 2.5K to ≈ 10K and again levelling out at $\approx 430 \pm 20$K, which could again be the result of the sample reaching the Néel temperature. Over the whole range from 2.5K to 500K the AR signal in L1 decreases from a value of 0.141 ± 0.001 to 0.021 ± 0.001. Where the red and green data sets meet at 300K they have values of 0.041 ± 0.001 and 0.040 ± 0.001 respectively. The difference between the signals of the green and dark blue data at 305K is 0.017 ± 0.001 and the difference between the dark blue and purple signals at 312K is 0.021 ± 0.002. In comparing the data for L1 to L2 it is illustrative to calculate the relative values, at 2.5K the L2 signal is $\approx 85\%$ the size of the L1 signal, this compares to $\approx 85\%$ at 300K, this suggests that both samples are behaving the same just with differing initial amplitudes.

In order to ascertain whether the AR signal is driven by the AFM order or simply by the changing resistivity, the temperature variation in $R_{yx} - R_{xy}$ has been plotted in Figure 18. Qualitatively it is clear that the unnormalised AR signal varies significantly less than the normalised signal in Figure 17 and in the opposite direction. As with Figure 16 and Figure 17 there is an indicator as to the value of the Néel temperature at the small humps in the blue and purple traces, which are centred on 433 ± 7K for the dark blue line and 433 ± 10K in the purple plot. Note that there is the small vertical line in the blue trace at 500K. This is a result of the system recording data past the point at which 500K was reached and shows the signal tending towards the value which would later become the end point for the purple line, this feature is also present in Figure 17 but cannot be seen at the scale of the Figure.

Over the range of 2.5K to 500K the value of $R_{yx} - R_{xy}$ changes from $2.96 \pm 0.01\Omega$ to $11.7 \pm 0.1\Omega$. At 305K the values for the green, blue, and purple traces at 312K are $4.59 \pm 0.01\Omega$, $7.64 \pm 0.02\Omega$, and $10.74 \pm 0.03\Omega$ respectively. At 440K the green, dark blue and purple traces have values of $5.8 \pm 0.1\Omega$, $9.7 \pm 0.1\Omega$, and $12.5 \pm 0.1\Omega$ respectively. These values correspond the a very

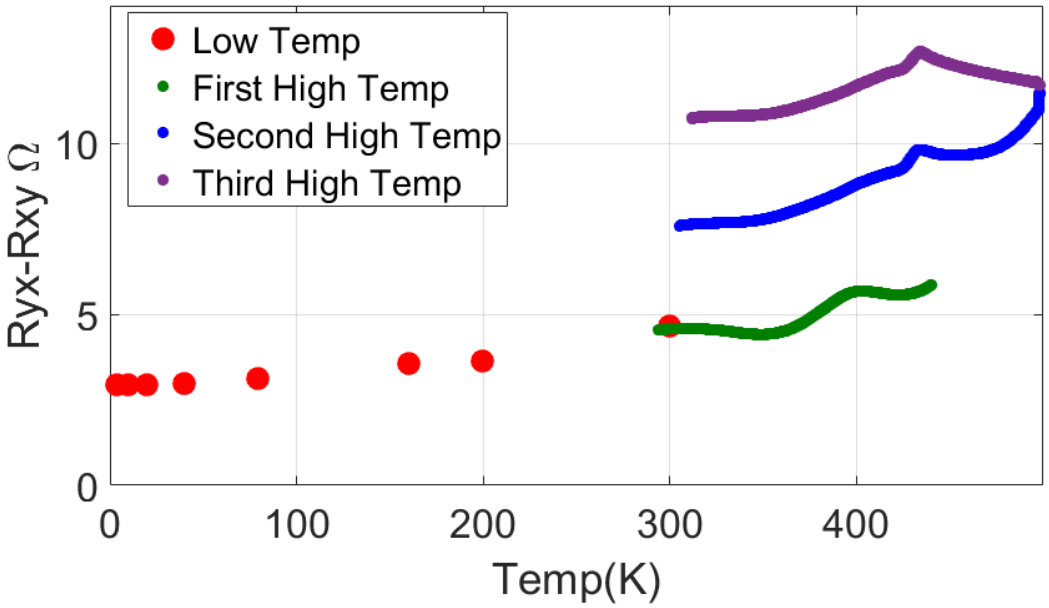

Figure 18: The unnormalised signal measured in L1 over the temperature range 2.5K to 500K.

significant increase in the unnormalised resistances of the sample once it has been heated to 440K and then again to 500K. At 300K the size of the signal increases by $\approx 2.1\times$ between the green and purple signals.

Dynamic Force Microscopy Results

The DFM images for the GaP side show a flat surface with a fairly uniform roughness, excluding two large dust particles, one of which was measured at a height of 0.25µm. The RMS roughness was taken from the top right corner, excluding the two largest features and the roughness in the height map was measured as 2.23nm and the amplitude map gave an RMS roughness of 352pm.

The images for the Al cap above CuMnAs are shown in Figure 19 where large dust particles were identified on the left middle across all images. The regions either side of the dust particles measure slightly lower than the surface scans before and after. This is an effect of the drastic change in tip height when scanning at the scan rate used and is therefore an artefact. The dust particle in the middle left of panel c) is a similar size to the dust on the GaP surface at 0.27µ. Otherwise this scan showed a very level surface with no step edges or detectable cracks. There are some scarring artefacts in the images, due to the rate of scan as well.

There is a diagonal streak in Figure 19a with a height of 3.2 ± 0.3Å, approximately half a unit cell of CuMnAs suggesting that an As terminated island of CuMnAs has formed. This is thought to be the case since, although the Al capping layer does have defined thickness, it follows the form of the CuMnAs surface very well [25]. The diagonal streak suggests some level of directional formation of islands, however without more images it is not possible to say whether they form predominantly in a single direction.

All of the amplitude images acquired show very little roughness and have a much reduced maximum feature height, 25nm compared to 0.27µm. The amplitude images also show reduced contrast in regions of large change and don't show islands. This means that the amplitude images

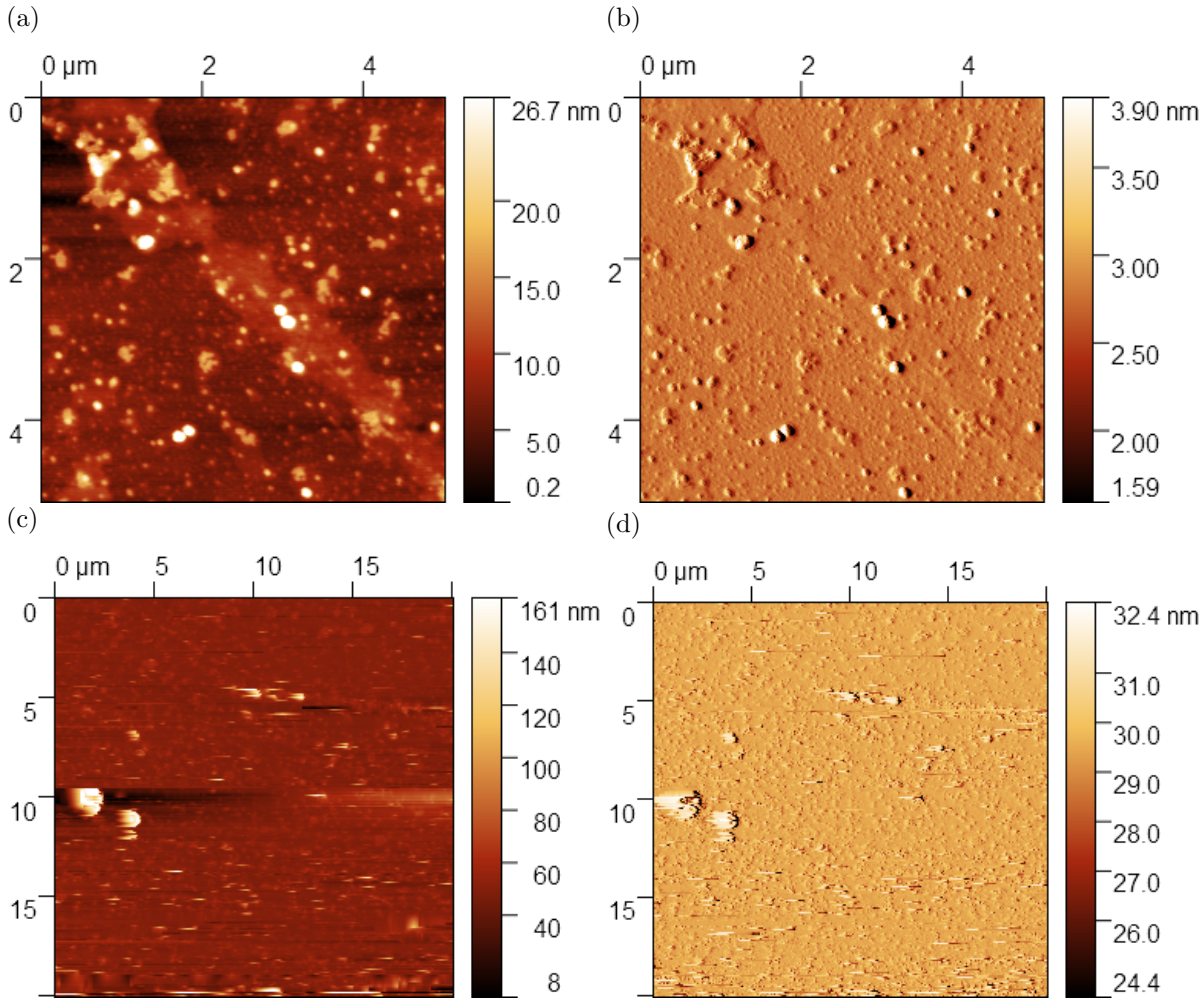

Figure 19: DFM images of the CuMnAs surface. a) Is the height retrace image for a 5um x 5um region of CuMnAs. The RMS roughness in a region in the upper left corner was found to be 3.26 nm. b) The amplitude map corresponding to the same region. The RMS roughness was found to be 226pm using the same pixels. c) Is the height retrace of an 20µm x 20µm region of CuMnAs. The RMS roughness for the top left corner was found to be 4.5nm. d) Is the height retrace for the same region and the RMS roughness was found to be 548.7pm using the same pixels.

are not useful for measuring defects or identifying the features we were looking for, however they have use in identifying and locating dirt and large features on the surfaces. They look much cleaner, and it would be nice if they could identify the features we wanted, however the reason they are cleaner is that the measurement is less sensitive, and so would be unhelpful for discovering cracks and other defects.

Simulation Results

In the process of building a simulation capable of modelling the behaviour of domain walls in AFMs, we found a number of other results which became pertinent to our discussion of AR and spin-flop, as well as AFMs more generally. These results are presented in this section.

Spin Flop Simulation Results

When simulating spin-flop we plotted profiles for how the angles the moments made with the easy axis changed as a function of their position within the crystal. Below the spin-flop field the moments behaved as expected with the two sublattices making angles of 0° and 180° to the easy axis, but for fields larger than B_{sf} the moments began to take on a different profiles such as those shown in Figures 20a-c.

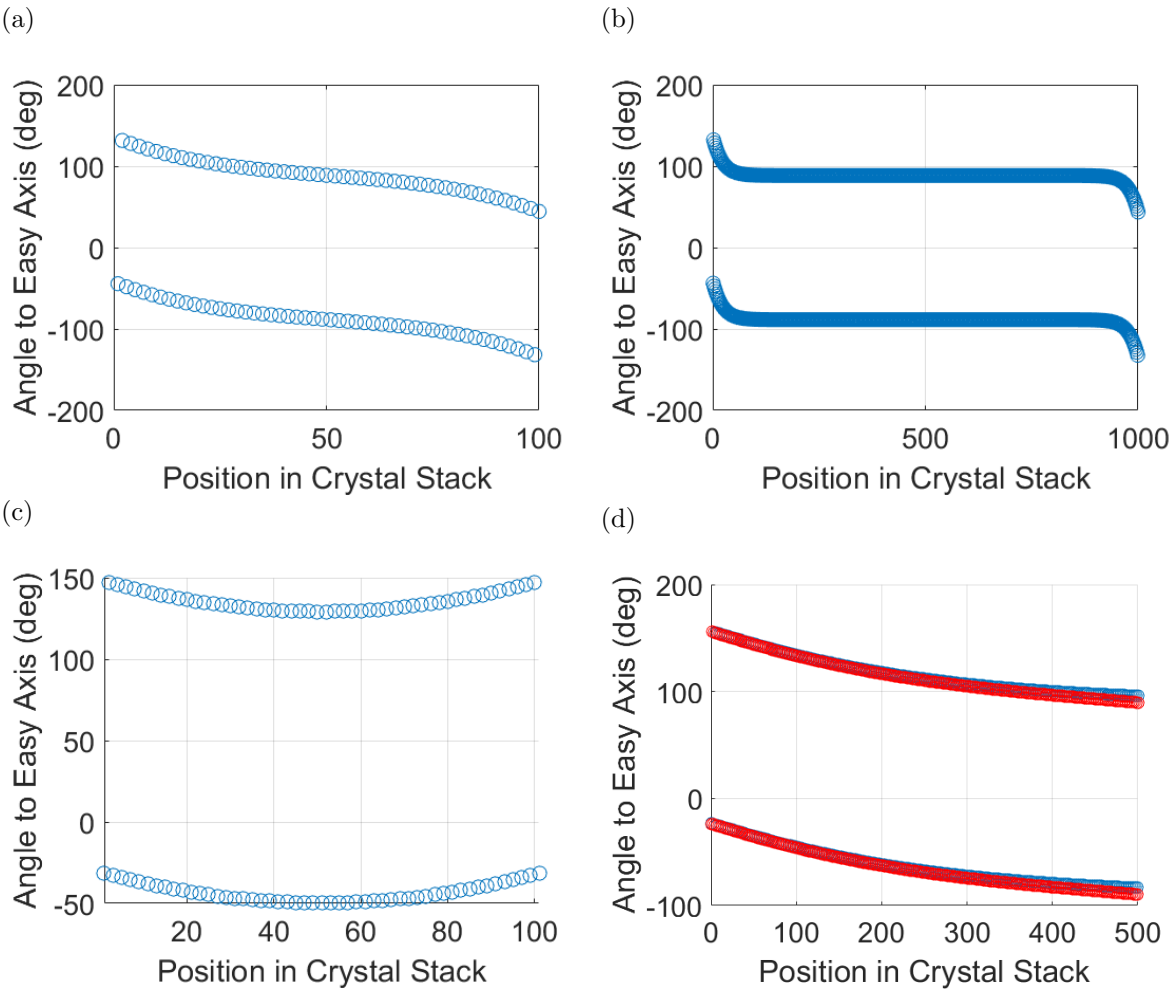

Figure 20: Plots showing the angle of moments in a 1D AFM crystal to the easy axis, in all examples $AM = 100\text{T}$, $\Delta/M = 0.01\text{T}$ and $t = 1000$. a) A profile with $n = 100$ and $B = 5\text{T}$. b) A profile with $n = 1000$ and $B = 5\text{T}$. c) A profile with $n = 501$ $B = 5\text{T}$. d) A profile between crustal index 1 and 500 for $n = 10000$ (blue) and $n = 1000$ (red) with $B = 2.4\text{T}$.

The profiles exhibit a curve towards the edge of the crystal whereby each moment is still $\approx 180°$ to its neighbour, but where the outermost in the crystal is canted towards the field by a far greater amount than its equivalent in the bulk. It is the outermost moment which

determines the direction in the curve at the crystal surface. With an even number of moments the system exhibits an antisymmetric profile whilst those with an odd number of moments display a symmetric one. This result is illustrated in Figures 20a and 20c. There is also another equivalent solution for all the plots in Figure 20 which can be obtained through a reflection in the $\theta = 0°$ axis, corresponding to solutions generated from differing initial conditions.

It can be seen from a comparison of Figures 20a and b, that the curvature at the edges of the crystal becomes a smaller proportion of the crystal as the crystal's size increases. In order to see if the edge followed approximately the same form in crystals with increasing size, solutions were found with $n = 1000$ and $n = 10000$, with the angles of the first 500 moments of each plotted in Figure 20d. Comparison of the red and blue lines in Figure 20d indicate that they follow a very similar form, with the two only deviating near the very centre of the $n = 1000$ crystal where the far edge only influences the smaller crystal.

Beyond the shapes of the profiles in Figure 20, there is also a difference in the bulk between those systems containing an odd and even number of moments. Upon comparing the centres of Figs. 20a and c, it can be seen that in even systems the moments lie at $\approx \pm 90°$ to the easy axis, whereas those in the odd system lie at angles of $\approx -50°$ and $\approx +130°$ to the axis. This is as a result of odd crystals containing one loose moment which leads to a net magnetisation in the unfloped crystal without an exchange interaction penalty, thus breaking the symmetry between the two sublattices. This is in contrast to the even case where the exchange coupling always acts to suppress any net magnetisation.

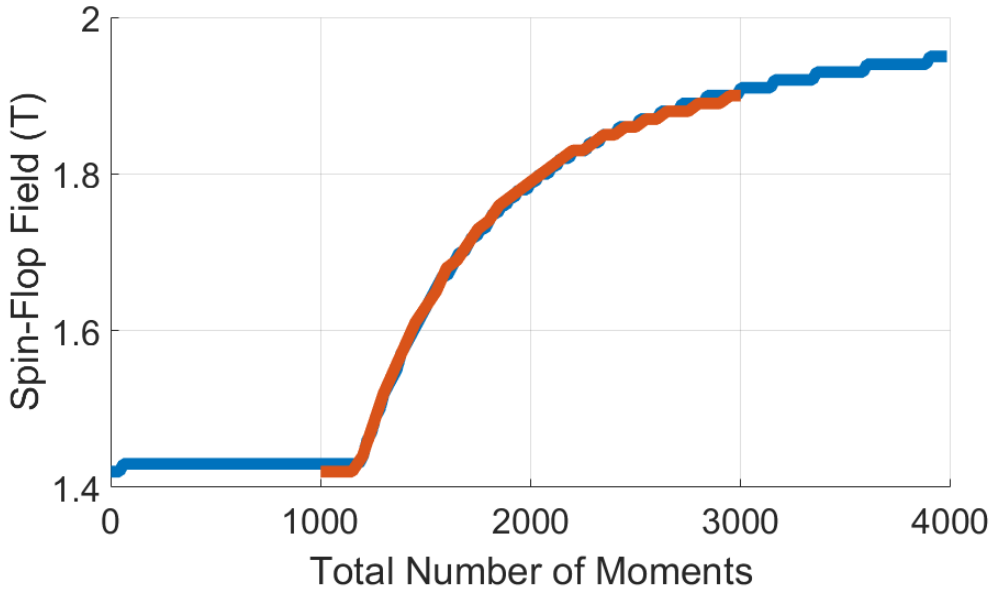

Figure 21: Plot of how B_{sf} varies with n, the blue curve is data in he range $2 - 4000$ in steps of 20 with $t = 10000$ and the orange is for the range $1000 - 3000$ in steps of 50 with $t = 4000$.

The difference between an odd and an even number of moments also becomes apparent when B_{sf} is calculated. When determining the spin-flop field with $AM = 100\text{T}$, $\Delta/M = 0.01\text{T}$ and $t = 4000$ a spin-flop field of $1.42 \pm 0.01\text{T}$ is obtained for any even $n < 1000$. By comparison in an odd system B_{sf} varies significantly for $n < 1000$. When n is very small and odd, the system does not undergo what would be recognisable as a flop since the sublattice with the greater number of moments remains aligned with the B field whilst the other sublattice rotates to align itself with the field when $B \approx AM$. When $n = 63$ and $AM = 100\text{T}$, $\Delta/M = 0.01\text{T}$ and $t = 10000$ the spin-flop field was determined to be $7 \pm 1\text{T}$, significantly higher than for $n = 64$. When

the number of moments is much larger however, the effect of the net magnetisation is relatively small. In the case where the number of moments is infinite, the solution must match that for an even number of moments. B_{sf} was determined in the infinite 1D case by considering a wrapped system, and with $AM = 100\text{T}$ and $\Delta/M = 0.01\text{T}$ the result is a B_{sf} of $2 \pm 0.01\text{T}$.

With the knowledge that that B_{sf} varies as a function of n, a plot was produced to demonstrate the form of the variation in an even crystal. The result of which for $AM = 100\text{T}$ and $\Delta/M = 0.01\text{T}$ is shown in Figure 21. The plot clearly shows that B_{sf} remains at $\sqrt{2}\text{T}$ until ≈ 1000 moments, at which point it begins to increase suddenly before tending towards its final value of 2T. The jaggedness in Figure 21 is as a result of the step process which selects an initial value for B to be just below the B_{sf} for the previous n, and the small random offset applied to the initial conditions. The randomness is therefore likely responsible for the small jump at the start of the blue curve.

Finally a spin-flop simulation was also carried out in 2D wrapped system with an exchange interaction as defined in Figure 5a, with $A_{\text{inter}}M = 50\text{T}$, $A_{\text{intra}}M = 150\text{T}$, $\Delta/M = 0.01\text{T}$ and $t = 20000$. The measured spin-flop field was then $B_{sf} = 2.88 \pm 0.01\text{T}$, which compares the expected result from Equation 30 of $B_{sf} = 2\sqrt{2} = 2.83\text{T}$.

Domain Wall Simulation Results

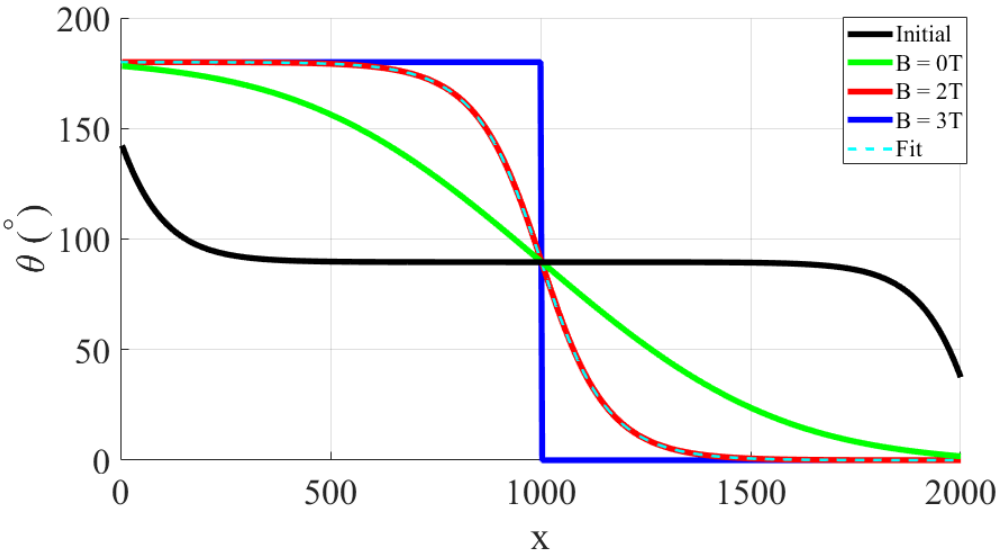

Figure 22: Plots of the angle dependence of moments in one sublattice as a function of position. The blue line indicates the initial conditions provided. The red line shows the result of the simulation with no external field. This is overlaid with the prediction by Equation 32. The result for an applied field below B_{sf} is displayed by the green line and the black line shows the domain wall in the flopped state.

The domain wall simulation required verification through comparing the results to the prediction of analytical solutions. To do this, a one dimensional simulation was conducted. First the value of δ_0 was varied by changing the value of A and the free fit parameter was compared to the value used. These agreed very well for all values of A used. Next the value of Δ was varied with a constant A. For larger values of Δ this held in good agreement however for lower values, the simulation did not match δ_0 well since the simulation required a higher value of t than was feasible. A value of Δ and A from the middle range of the values was chosen to be used for the rest of the simulations. This value was $\delta_0 = 100$ using $\Delta/M = 0.01\text{T}$ and $AM = 100\text{T}$. The

resulting domain wall is the red line in Figure 22 and the free fit parameter was used to plot the dashed cyan line, which overlays the red line.

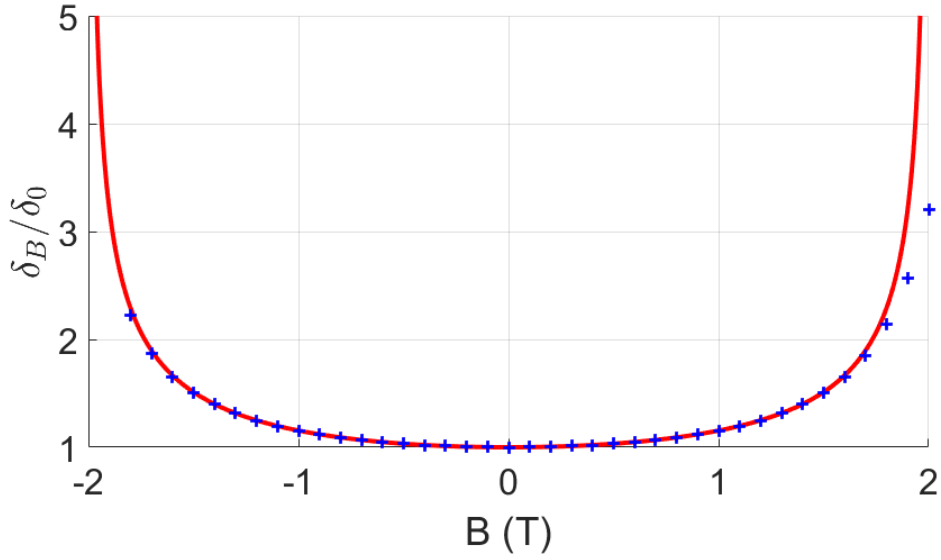

Figure 23: Plot of the observed domain wall width with increasing field and the prediction according to Equation 34. The blue plus symbols represent the ratio of domain wall width parameters $\frac{\delta_0}{\delta_B}$ as a function of applied field along the easy axis. The red line shows the predicted width ratios.

Increasing magnitude fields were applied along the easy axis of the one dimensional chain. This resulted in a widened domain wall for fields below B_{sf}. For a field above B_{sf}, all moments away from the edges flopped and the domain wall seemed to split into two walls at the edge as shown by the black line in Figure 22. This is identical to the behaviour in the 1D spin flop simulation. A field was systematically applied and the free fit parameter δ_B was recorded. These values were compared to the prediction made by Equation 34 with $h = B/2$ and are shown in Figure 23. As can be seen, the fit is very good below ≈ 1.6T. Above this field, the curve starts to diverge faster than the data as the predicted value of δ_B becomes complex.

Topological defects do not form in 1D chains and so the 2D and 3D models were used to investigate these. The rate of formation was compared between small randomness and large randomness in the initial conditions. Using random offsets of normally distributed angles between -0.025 and 0.025° at first, topological defects formed regularly but only one or two per 64 FM layers. Using values of -25 to 25° generated several defects within a single wall every time, typically 3 or 4. A value of $\pm 0.25°$ was chosen as the random offset for every other domain wall simulation.

A two dimensional domain wall was formed with $A_{\text{inter}} = 50$T and $A_{\text{intra}} = 150$T. The anisotropy strength was unchanged, using $\Delta = 0.01$T. The steady state solution was found for a predetermined chirality model and the domain wall was fit using the profile of one of the ferromagnetic layers near the centre. The domain wall width was found to be $\delta_0 = 70.71...$ which corresponds to $A_{\text{fit}} = 50$T. This suggests that the weaker coupling strength determines the width of the domain wall.

The presence of topological defects dramatically reduced the width of the domain wall, as can be seen by comparing the contours of equal angle in panels 24a and b to those in 24c and d. Small gaps between defects allow for only a thin wall to form between them. With larger gaps, the width of the wall between defects can approach the width of a wall without defects.

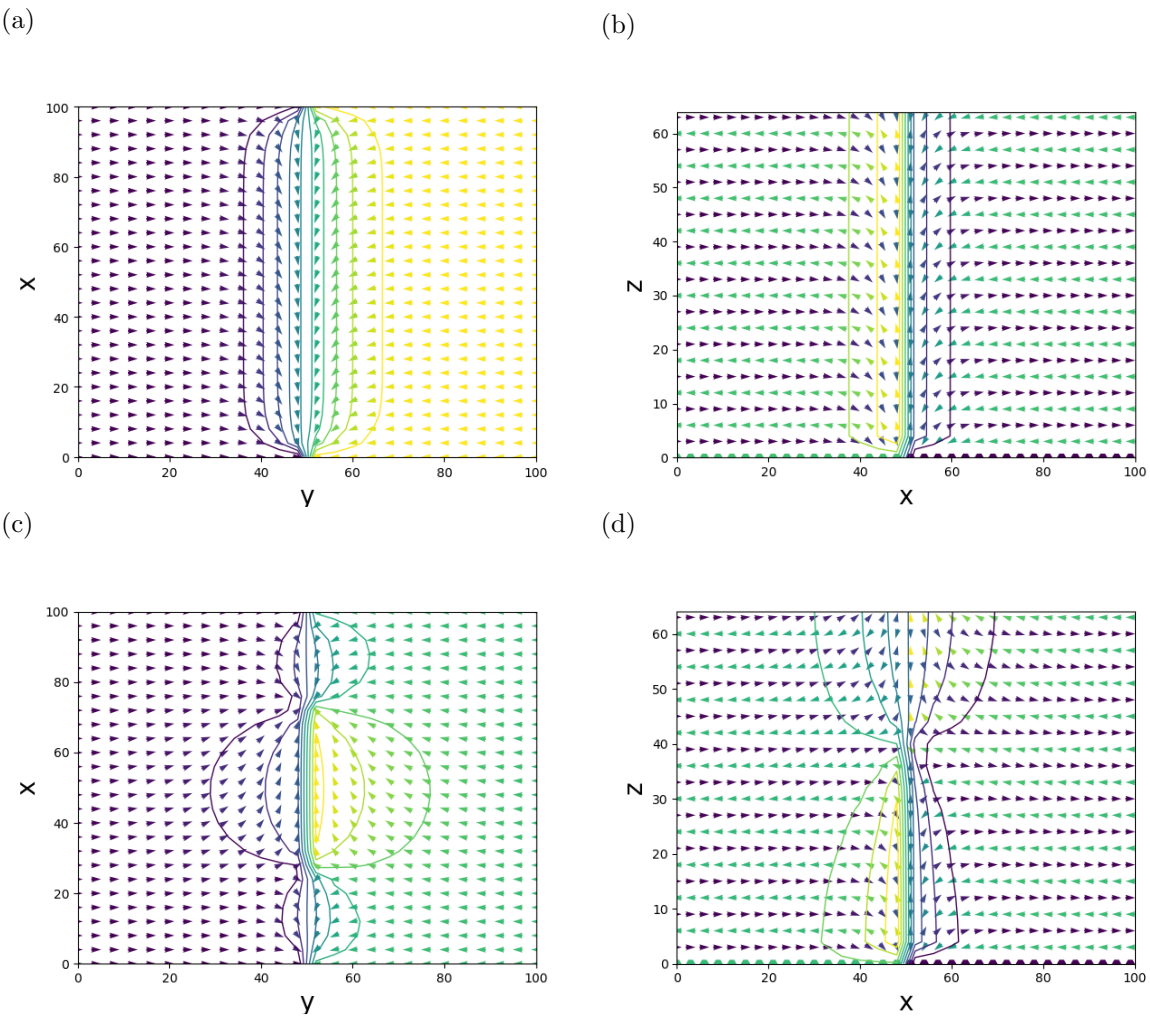

Figure 24: Vector plots of moments in a lattice for comparison between lattices with and without topological defects. a) Shows a slice in the x-y plane for a system with predefined chirality where b) Shows a similar slice in the x-z plane. c) Shows a slice in the x-y plane for a crystal with topological defects and d) Shows a slice of the same crystal in the x-z plane. The vector arrows represent the direction of magnetisation of the moments in that region and the contours are lines of equal angle.

The x-y plane view of the domain wall shows thinning of the domain wall at the edge, forming a lens shape. This so called lensing is produced by the lower exchange energy at the edge (since the edge has no moments). This results in a smaller value for δ_0 at this point, since the exchange energy is effectively halved.

Anisotropy and Exchange Strengths

Using our experimentally determined value for the spin-flop field in L1 of $B_{\mathrm{sf}} = 1.48 \pm 0.04\mathrm{T}$, we can obtain an expression relating to the product ΔA in two limits. The first limit is that of a small crystal, which our spin-flop simulations demonstrate have a spin-flop field given by Equation 16 as $B_{\mathrm{sf}} = \sqrt{2\Delta A_{\mathrm{av}}}$. The other limit is for a bulk crystal for which CuMnAs has a spin-flop field defined by Equation 31 as $B_{\mathrm{sf}} = 4\sqrt{\Delta A_{\mathrm{av}}}$.

The XMLD-PEEM images of our CuMnAs sample [22] provide an estimate for the domain wall width of $\approx 0.1\mu\mathrm{m}$, which corresponds to approximately 300 unit cells and therefore 300 moments. This would suggest a value of $\delta_0 \approx 150 \pm 50$ moments. This width can be related to the ratio of the exchange to the anisotropy strength via $\delta_0 = M\sqrt{A/\Delta}$. Our results in domain wall simulation suggest that the exchange constant in the expression is A_{inter}, and we can rewrite the expression using $2A_{\mathrm{inter}} = A_{\mathrm{av}}$ to give $\delta_0 = M\sqrt{A_{\mathrm{av}}/2\Delta}$.

By multiplying the expressions for δ_0 and B_{sf} we can find values for the exchange an anisotropy strengths. For a small crystal the product gives $\delta_0 B_{\mathrm{sf}} = MA_{\mathrm{av}}$, and for a bulk system the product is $\delta_0 B_{\mathrm{sf}} = 2\sqrt{2}MA_{\mathrm{av}}$. Using our value for the spin-flop field and the XMLD-PEEM data, the exchange coupling strength is found as $MA_{\mathrm{av}} = 220 \pm 70\mathrm{T}$ in a small crystal, with an anisotropy strength of $\Delta/M = 0.005 \pm 0.002\mathrm{T}$. For the solution in a bulk crystal the exchange strength is calculated as $MA_{\mathrm{av}} = 80 \pm 30\mathrm{T}$, with a corresponding anisotropy strength of $\Delta/M = 0.0015 \pm 0.0005\mathrm{T}$.

Discussion

We are confident that we were able to observe a spin-flop transition in both samples of CuMnAs, with a value for the spin-flop field obtained of $B_{\text{sf}} = 1.48 \pm 0.04$T in L1 and $B_{\text{sf}} = 1.44 \pm 0.08$ in L2 at 2.5K. By performing field sweeps at multiple angles we were able to confirm that the sample was uniaxial as expected.

Using our measured spin-flop fields and the XMLD-PEEM data we we able to produce rough values for the exchange coupling strength and the anisotropy strength in the two limits of a small sample and an infinite sample. The two sets of solutions set a range for the possible values of between 80 ± 30T and 220 ± 70T for the exchange strength, and between 0.0015 ± 0.0005T and 0.005 ± 0.002T for the anisotropy strength. The dominant source of error on these values is the XMLD-PEEM data, as the resolution of the image imposes a large uncertainty on the domain wall width. It was also not possible to fit any profile to find δ_0 accurately, as a result of both resolution and the sample containing walls of varying width. We do not know which of the limits used is closer to the true solution as although our sample is only ≈ 64 moments thick, it is much larger in the other two directions (> 10000 moments) and we were not able to perform a simulation for a system of similar dimensions due to limited computational power.

The most significant assumptions in calculating the range for the anisotropy-exchange product are the uniformity of the anisotropy term throughout the sample, that the sample single domained, and for the upper limit that we used an equation which only applies for an even number of moments. In reality the first two of these are very unlikely, with the anisotropy changing with increasing thickness to make the sample biaxial and domain walls having been imaged in the RC123 sample [22]. We should also consider the effect of the difference between an odd number of moments, this becomes important when step edges are present in the sample as the region on one side could experience a larger spin-flop field than the other, the spin-flop field would then be altered depending on the cost associated with a 90° domain wall. Although, the fact that the spin-flop field seems to be consistent with other samples of CuMnAs, with spin flop in the range $1 - 2$T [35], would tend to suggest that difference between an odd and even number of moments may be insignificant at this scale. This would point to the bulk solution providing the correct value. The spin-flop field may, however, still be a function of the surface step edge density which could be consistent between the considered sample. This could by investigated further in samples with non-constant thickness.

Another point of note in the spin-flop profile is the soft nature of the transition, as for a field perfectly aligned with a single domained sample a discrete flop would be expected. The soft nature of the flop in L2 could be a result of sample misalignment which was investigated through the rotation of our sample. The L1 sample however appeared well aligned to within the error of our crude rotation setup. The softness in L1 could be the result of multiple factors, we suspect that domain walls play a critical role as our simulations indicate that they flop by slowly widening rather than undergoing a discrete flop.

In attempting to understand the AR signal the most surprising result is the difference between the spin-flop amplitude and the zero field AR signal, with the zero field signal being $\approx 100\times$ greater. Whats more is the fact that the zero field signal decreases by a factor $\approx 1/3$ at 150K whereas the spin-flop signal is almost unchanged. This suggests one of two possibilities, the first is that the AR signal is not solely a magnetic phenomena, with an anisotropic crystallographic contribution playing a part, or that the arrangements of moments in the flopped and/or unflopped states are significantly different from that expected in the simple single domain picture. We believe that crystallographic contributions are unlikely to be the cause due to the agreement between samples L1 and L2 in both spin-flop and temperature variant measurements. The most obvious cause is then that of a complex domain structure. The 90° domain walls appear as a prime

candidate as they would only become apparent above the spin-flop field, which would explain the relatively large zero-field signal.

We are confident in the estimates gained from the AR measurements for the Néel temperature of 440 ± 10K and 430 ± 20K which is lower than the 480 ± 5K reported in a thicker 500nm sample [12], we would suggest the difference is a result of the changing form for the magnetic anisotropy with thickness. Levelling off of the AR signal in Figure 17 when this presumed Néel temperature is reached would indicate that the signal has some magnetic contribution, whilst a non-zero value at this point indicates that there are also additional contributions, which are either non-magnetic in origin or have a greater magnetic ordering temperature. There is also a feature associated with this point in both constituent parts to the AR signal, with a slowing for the increase in ρ_{xx} with temperature and a small hump for the non-relative AR signal. This would suggest that there is some magnetic significance to this temperature, and the decrease seen in the purple plot of Figure 18, may be indicative of a decreasing magnetic order as the temperature is raised above this temperature.

One significant observation to be made in the AR data is the increasing signal size for samples which had already been taken up to 440K and then up to 500K, bringing the non-relative AR signal up to $\approx 2.1\times$ its initial value. This cannot be a result of annealing as it is driving an increase in the unnormalised signal, and has little impact upon the resistivity. The possible causes for this signal might be the reorganisation of the magnetic order when above the Néel temperature. This could include a reorganisation of the domain structure or be a result of the removal of some topological domain wall defects at high temperature. It could also be the result of the interface between the GaP substrate and CuMnAs changing which may act to alter the anisotropy strength. The uncertainty in the explanation for this phenomena would indicate that further study is required to find the origin. One possible direction would be to take measurements of the AR signal back down to 2.5K. Retaking spin-flop measurements at 2.5K could also be insightful.

The images of the surface acquired using DFM showed fairly smooth surfaces with some dust and debris. Only one image showed any sign of an anisotropic defect, which we suggest is a surface island with a height of half the unit cell. None of the more significant features such as cracks were observed, this suggests that the sample has very few direction dependent defects which could be responsible for the AR signal. More scans could be taken to check if features similar to the observed island are found elsewhere. If this were to be done, a note of the crystallographic direction should be taken and shown on the images.

The quality of the image was determined by the setpoint value used. This value needed to be adjusted such that the forward and backward scans were consistent, however many times large defects would upset them and cause the image to scar or create significant noise. This can be avoided by cleaning the sample better or performing DFM in a dust free environment and by gaining more experience with choosing a setpoint for DFM.

The images were acquired at a constant rate of 0.2 lines per second, regardless of size. This meant that the image quality was much worse for larger scans. Ideally the rate would have been reduced for the large scans but the access time of the equipment was limited. Similarly, the integral gain value was 10 for all scans. This should have been around 30 for $20\mu m \times 20\mu m$ scans and 20 for $10\mu m \times 10\mu m$ scans [32].

In the course of conducting the simulations we gained a number of qualitative results in which we have a high level of confidence, as well as a number of numerical results in which we have a reasonable level of confidence. Figure 20 show the influence of the surface moments on the behaviour of the crystal when in the flopped state, this should have an influence on the size of the AR signal, but only in line with the proportion of moments in the edge of the crystal

and therefore not explaining the $\approx 100\times$ difference between AR and spin-flop signals. Far more significant for our experimental results is the realisation that systems containing an odd number of moments undergoes a spin-flop at a higher field than that for an even number. As an island of 3.2 ± 0.3nm in height was observed in the DFM image of RC123. It suggests that the formation of 90° domain walls above the spin flop field for the even region is a definite possibility. However as already discussed. It is likely that the sample is flopping in the bulk regime, in which case this would be less of a contributor.

We have reasonable confidence in our simulated spin-flop data. This is due to the agreement with the analytical results generated for 1D and 2D flop. The same is true for Figure 21 which shows agreement with the analytical results at $n = 2$ and tends towards the correct solution at $n = \infty$. The limit in these results however was the computational power available, as especially near the spin-flop field the system takes a long time to find the correct solution, with it taking $\approx$ 1week to simulate a single plot in Figure 21. To achieve better results it would be ideal to find the solution for multiple starting conditions such that the results from each could be used to arrive at a statistical average for the spin-flop field.

The domain wall simulations conducted functionally predicted the width, with two different analytical solutions matching our value in zero field conditions almost perfectly. The fact that the prediction matches very well for the various values of δ_0 used inspires confidence. The result with applied fields matched well for the one value of δ_0 used. It should also be noted that the field in the original equation, h, was found to relate to the magnitude of field we used as $B = \frac{h}{2}$ and we do not know the origin of this factor of $\frac{1}{2}$ difference [30]. With this correction however, the fit is very good until the field is close to the maximum field of 2T determined by the square root in Equation 34. Here, the value starts to deviate from the prediction slightly. This could very likely be due to the total virtual time, t, being too low. The value of t used was $t = 2000$ because this was found to be sufficient for a field of 1T, which was the original intended limit. The field was then set to larger values and the value of t was not increased accordingly.

Representing the bonding of nearest neighbour moments in 2D and 3D using arrays posed a challenge. In a square lattice, if one moment, i, is above and to the right of moment j by one lattice site, then moment j is below and to the left of i. This is not true when representing the moments in CuMnAs using a single matrix as was done in the simulation. This is because if i is above and to the right of j, then j can be chosen to be any other direction within one position so long as the relative arrangement is consistent. In our case, i was directly below j. Without doing this, the wall forms diagonally because the moments are not offset by an appropriate amount to have the correct nearest neighbours. It would be possible to double the size of each dimension for the matrix and fill the gaps with empty or null values, to use two separate matrices or to take the approach we took.

The lack of any thermal contributions in the model reduces the accuracy of the simulation because topological defects cannot relax and spin flop cannot occur because the energy barrier cannot thermally be overcome as it should be able to. That being said, the spin flop can occur if started in a flopped state as well as unflopped. This approach does not work for other applications, such as randomly generated domains for which a Monte-Carlo simulations excel. This is because the ODE approach changes every moment between energy calculations where the Monte-Carlo simulation will randomly choose a moment and evaluate that moment's energy for its original angle and a randomly chosen angle. The angle of that moment is then replaced with the angle which corresponds to the lower of the two energies. This approach very much avoids spin flop because only one moment is updated at a time.

It may be possible to introduce thermal effects into the ODE method however the way that an ODE solver determines the successfulness of a step is complicated and so adding randomness to the solutions could be detrimental to the result or just cause an error in the program.

The observation of lensing in other magnetic materials has been investigated and is usually attributed to magnetostrictive effects which are compressive or constrictive forces. The forces are generated by the interactions between each moment in the lattice such that in a large domain the sum of all the interactions between neighbours generates a strain in the material. The domains often break apart to alleviate the stress [36]. Magnetostriction is not incorporated into our simulation in any way. In the case of our simulations, the lensing observed in the x-y plane is caused by an increased anisotropy at the edges. This anisotropy increase is only due to the lack of exchange at the edge which reduces the strength of the field acting to align the moment anti-parallel to its neighbours, resulting in a larger ratio of anisotropy to exchange energy.

Simulating magnetostriction is possibly as simple as having a nearest neighbour interaction energy which can be calculated for each moment, similar to the exchange energy in our model. If it is this simple, the next step is clearly to add this and observe the effects on the material. This may, however, require allocating a position to each moment as well, and allowing this position to be updated by the stress in the material and thus generating a strain as well. Instead, a strain field may be more applicable.

When considering how to include further contributions such as magnetostriction and thermal contributions, it must be made clear that before this is feasible, the simulation needs to be heavily optimised, especially if three dimensions are desired. In order to do $100\times100\times64$ simulation with $t = 1000$ took several days. Attempts to improve the efficiency while still using MATLAB's ode45 function were unsuccessful. A significant problem is the limitation that requiring two 1D vector inputs, one of time and the other of the working values of the variable to be solved. If it took ND matrices this would be a lot more versatile.

An attempt was made to vectorise (or linearise) the calculation by creating sub arrays which were the original array shifted such that each element of the original array corresponds to the element of the nearest neighbour moment in a chosen direction. This allows for a single matrix calculation to be done for each energy term. This was done for all eight nearest neighbours for a three dimensional simulation but ended up slowing down drastically due to making so many arrays repeatedly. In order to speed this up, the array needed to have it's values updated at the end of the evaluation instead of being remade at the start of each evaluation loop. This would require writing a new ODE solver which is outside the scale of this project.

If the vectorising approach is taken, it would seem sensible to use the graphics processing unit (GPU) of a computer to speed it up. This is possible in MATLAB using the gpuArray package, however the ODE solvers provided by MATLAB do not take arrays stored on the GPU as inputs and so writing to the GPU memory and then reading off it again was done for each energy evaluation. Input and output operations with the GPU are very slow and so this slows the reading and writing its memory is dramatically slower than the normal approach. The only foreseeable way to improve the performance is by writing code for the GPU, using CUDA, OpenCL, OpenGL or any other GPU interfacing language. Again, this is outside the scope of this project but may have significant improvements in performance if written well.

If the simulation was faster, two dimensional and three dimensional domain walls could be considered in field, allowing study into its effect on domain wall structures not present in 1D. Possible directions could be, including a set number of defects in various positions, changing the density of defects or introducing an odd number of antiferromagnetic layers. Fields could also be applied along different directions since applying along the hard axis should cant moments outside of the wall and thin the domain wall itself. It would be interesting to see how this compares to analytical predictions.

The simulation could also be used to investigate the effects of different forms of the GaP induced anisotropy. It is expected to decay away from the GaP surface and so thicker materials are

biaxial with thin materials being uniaxial. It could be interesting to introduce different rates of exponential decay, trying different powers and comparing to a simple cut-off point or linear form. There is much to be done in order to compare this to the real sample, however.

Ideally the simulations would be a dynamic simulation of the moments as oscillating spins, incorporating magnetostriction, exchange, anisotropy, applied fields, temperature and anything else induced by the environment the moments are in. This would allow the investigation of phenomena such as spin-transfer torque and more accurately describe domain wall motion. However this represents a major computational challenge and would most likely be limited to a small number of moments, without significant optimisation.

Summary

This report aimed to investigate some of the inrintrinsic magnetic properties in CuMnAs. The origin of the anisotropic resistances and the spin flop field were of particular interest. Both experimental works and simulations were conducted in an attempt to probe such properties and were partially successful. We found an estimate a range of the anisotropy and exchange energy densities of between 80 ± 30T and 220 ± 70T, and between 0.0015 ± 0.0005T and 0.005 ± 0.002T respectively. We have shown that anisotropic magnetoresistance is likely a significant contributor to the anisotropic resistance values, however may not be the only contributor. The zero field signals were $\approx 100\times$ greater than any anisotropic resistance signal, which we suggest is the result of a complex domain wall structure. We also demonstrated the large increase in the anisotropic resistance signal associated with samples which have been taken up to the Néel temperature, a phenomenon which could be investigated further and could give further insight into the nature of the anisotropic resistance signal.

The simulations successfully predicted both the spin flop field and the domain wall width for theoretical antiferromagnetic crystals. The significance of surfaces on the spin flop has clearly been shown to reduce the anisotropic magnetoresistance signal, having an odd number of moments was shown to significantly increase the spin flop field and topological defects were shown to reduce domain wall width. We believe that the model is ready for further applications in investigating the effects of applying fields to 2D and 3D domain walls, of introducing non-magnetic defects in the lattice and many other effects. The useful qualitative results gained could hopefully be further developed to allow more accurate depictions of a real crystal, which would allow for quantitative comparison between the simulation and experimental results.

The combination of experimental and numerical results obtained provide fertile ground for future research, and hopefully contribute to a greater understanding of CuMnAs as well as antiferromagnets more generally.

References

[1] M. L. Néel, "Propriétés magnétiques des ferrites; ferrimagnétisme et antiferromagnétisme," in *Annales de Physique*, vol. 12, pp. 137–198, 1948.

[2] M. N. Baibich, J. M. Broto, A. Fert, F. N. Van Dau, F. Petroff, P. Etienne, G. Creuzet, A. Friederich, and J. Chazelas, "Giant magnetoresistance of (001) fe/(001) cr magnetic superlattices," *Physical review letters*, vol. 61, no. 21, p. 2472, 1988.

[3] P. Wiśniewski, "Giant anisotropic magnetoresistance and magnetothermopower in cubic 3: 4 uranium pnictides," *Applied physics letters*, vol. 90, no. 19, p. 192106, 2007.

[4] D. C. Ralph and M. D. Stiles, "Spin transfer torques," *Journal of Magnetism and Magnetic Materials*, vol. 320, no. 7, pp. 1190–1216, 2008.

[5] M. N. Baibich, J. M. Broto, A. Fert, F. N. Van Dau, F. Petroff, P. Etienne, G. Creuzet, A. Friederich, and J. Chazelas, "Giant magnetoresistance of (001) fe/(001) cr magnetic superlattices," *Physical review letters*, vol. 61, no. 21, p. 2472, 1988.

[6] T. Jungwirth, X. Marti, P. Wadley, and J. Wunderlich, "Antiferromagnetic spintronics," *Nature nanotechnology*, vol. 11, no. 3, pp. 231–241, 2016.

[7] C. Chappert, A. Fert, and F. N. Van Dau, "The emergence of spin electronics in data storage," *Nature materials*, vol. 6, no. 11, pp. 813–823, 2007.

[8] K. Olejník, V. Schuler, X. Martí, V. Novák, Z. Kašpar, P. Wadley, R. P. Campion, K. W. Edmonds, B. L. Gallagher, J. Garcés, *et al.*, "Antiferromagnetic cumnas multi-level memory cell with microelectronic compatibility," *Nature communications*, vol. 8, p. 15434, 2017.

[9] M. Hagiwara, K. Katsumata, H. Yamaguchi, M. Tokunaga, I. Yamada, M. Gross, and P. Goy, "A complete frequency-field chart for the antiferromagnetic resonance in mnf 2," *International journal of infrared and millimeter waves*, vol. 20, no. 4, pp. 617–622, 1999.

[10] V. Baltz, A. Manchon, M. Tsoi, T. Moriyama, T. Ono, and Y. Tserkovnyak, "Antiferromagnetism: the next flagship magnetic order for spintronics?," *arXiv preprint arXiv:1606.04284*, 2016.

[11] O. Gomonay, T. Jungwirth, and J. Sinova, "High antiferromagnetic domain wall velocity induced by néel spin-orbit torques," *Physical review letters*, vol. 117, no. 1, p. 017202, 2016.

[12] P. Wadley, V. Hills, M. Shahedkhah, K. Edmonds, R. Campion, V. Novák, B. Ouladdiaf, D. Khalyavin, S. Langridge, V. Saidl, *et al.*, "Antiferromagnetic structure in tetragonal cumnas thin films," *Scientific reports*, vol. 5, 2015.

[13] N. Lou1s, "Magnetism and the local molecular field," *Physics, 1963-1970*, vol. 4, p. 318, 1998.

[14] T. Satoh, S.-J. Cho, R. Iida, T. Shimura, K. Kuroda, H. Ueda, Y. Ueda, B. Ivanov, F. Nori, and M. Fiebig, "Spin oscillations in antiferromagnetic nio triggered by circularly polarized light," *Physical review letters*, vol. 105, no. 7, p. 077402, 2010.

[15] A. Kimel, A. Kirilyuk, A. Tsvetkov, R. Pisarev, and T. Rasing, "Laser-induced ultrafast spin reorientation in the antiferromagnet tmfeo 3," *Nature*, vol. 429, no. 6994, p. 850, 2004.

[16] J. Železnỳ, H. Gao, K. Výbornỳ, J. Zemen, J. Mašek, A. Manchon, J. Wunderlich, J. Sinova, and T. Jungwirth, "Relativistic néel-order fields induced by electrical current in antiferromagnets," *Physical review letters*, vol. 113, no. 15, p. 157201, 2014.

[17] J. Železnỳ, H. Gao, A. Manchon, F. Freimuth, Y. Mokrousov, J. Zemen, J. Mašek, J. Sinova, and T. Jungwirth, "Spin-orbit torques in locally and globally noncentrosymmetric crystals: Antiferromagnets and ferromagnets," *Physical Review B*, vol. 95, no. 1, p. 014403, 2017.

[18] P. Wadley, B. Howells, J. Železnỳ, C. Andrews, V. Hills, R. P. Campion, V. Novák, K. Olejník, F. Maccherozzi, S. Dhesi, *et al.*, "Electrical switching of an antiferromagnet," *Science*, vol. 351, no. 6273, pp. 587–590, 2016.

[19] X. Marti, I. Fina, C. Frontera, J. Liu, P. Wadley, Q. He, R. Paull, J. Clarkson, J. Kudrnovskỳ, I. Turek, *et al.*, "Room-temperature antiferromagnetic memory resistor," *Nature materials*, vol. 13, no. 4, p. 367, 2014.

[20] D. Kriegner, K. Výbornỳ, K. Olejník, H. Reichlová, V. Novák, X. Marti, J. Gazquez, V. Saidl, P. Němec, V. Volobuev, *et al.*, "Multiple-stable anisotropic magnetoresistance memory in antiferromagnetic mnte," *Nature communications*, vol. 7, p. 11623, 2016.

[21] I. Fina, X. Marti, D. Yi, J. Liu, J.-H. Chu, C. Rayan-Serrao, S. Suresha, A. Shick, J. Železnỳ, T. Jungwirth, *et al.*, "Anisotropic magnetoresistance in an antiferromagnetic semiconductor," *Nature communications*, vol. 5, p. 4671, 2014.

[22] K. Edmonds, P. Wadley, S. Reimers, *et al.*, "Domain analysis of a 20nm cumnas sample," *University of Nottingham*, 2018. Unpublished manuscript.

[23] M. Grzybowski, P. Wadley, K. Edmonds, R. Beardsley, V. Hills, R. Campion, B. Gallagher, J. S. Chauhan, V. Novak, T. Jungwirth, *et al.*, "Imaging current-induced switching of antiferromagnetic domains in cumnas," *Physical review letters*, vol. 118, no. 5, p. 057701, 2017.

[24] T. McGuire and R. Potter, "Anisotropic magnetoresistance in ferromagnetic 3d alloys," *IEEE Transactions on Magnetics*, vol. 11, no. 4, pp. 1018–1038, 1975.

[25] V. A. Hills, *MBE growth, characterisation and physics of antiferromagnetic copper manganese arsenide*. PhD thesis, University of Nottingham, 2016.

[26] F. Máca, J. Kudrnovskỳ, V. Drchal, K. Carva, P. Baláž, and I. Turek, "Physical properties of the tetragonal cumnas: A first-principles study," *Physical Review B*, vol. 96, no. 9, p. 094406, 2017.

[27] C. Kittel, "Physical theory of ferromagnetic domains," *Reviews of modern Physics*, vol. 21, no. 4, p. 541, 1949.

[28] F. Bloch, "On the theory of the exchange problem and the remanence phenomenon of ferromagnets," *Z. Phys*, vol. 74, p. 295, 1932.

[29] S. Rohart and O. Fruchart, "A few analytical micromagnetic problems," *Tutorial from The European Magnetism Association*, 2011.

[30] N. Papanicolaou, "Antiferromagnetic domain walls," *Physical Review B*, vol. 51, no. 21, p. 15062, 1995.

[31] S. S. Parkin, M. Hayashi, and L. Thomas, "Magnetic domain-wall racetrack memory," *Science*, vol. 320, no. 5873, pp. 190–194, 2008.

[32] R. Fuierer, "Procedural operation manualette," *Asylum Research*, 2009.

[33] R. Garcıa and R. Perez, "Dynamic atomic force microscopy methods," *Surface science reports*, vol. 47, no. 6-8, pp. 197–301, 2002.

[34] P. Wadley, V. Novák, R. Campion, C. Rinaldi, X. Martí, H. Reichlová, J. Železnỳ, J. Gazquez, M. Roldan, M. Varela, *et al.*, "Tetragonal phase of epitaxial room-temperature antiferromagnet cumnas," *Nature communications*, vol. 4, p. 2322, 2013.

[35] M. Wang, C. Andrews, *et al.*, "Spin flop in antiferromagnetic cumnas," *University of Nottingham*, 2018. Unpublished manuscript.

[36] M. Doerr*, M. Rotter, and A. Lindbaum, "Magnetostriction in rare-earth based antiferromagnets," *Advances in Physics*, vol. 54, no. 1, pp. 1–66, 2005.